Science Advances

MAAAS

Supplementary Materials for

Building block properties govern granular hydrogel mechanics through contact deformations

Dilara Börte Emiroglu *et al.*

Corresponding author: Mark W. Tibbitt, mtibbitt@ethz.ch

This PDF file includes:

Supplementary Text
Figs. S1 to S27
Tables S1 to S5
References

Supplementary Text

1. Mechanical Testing methods

1.1. *Fluid force microscopy (FluidFM)*

Force distance curves of hydrogels were acquired using fluidic force microscopy (FluidFM), which is an atomic force microscopy (AFM) based technique.(*37*) FluidFM setup consists of a FlexAFM-near-infrared scan head driven by the C3000 controller with the EasyScan2 software (Nanosurf AG, Switzerland), a pressure controller (Cytosurge AG, Switzerland), a hollow microfluidic probe (Cytosuge AG), and an inverted microscope (Axiovert, Carl Zeiss, Germany) with a CMOS camera (Hamamatsu ORCA-Flash camera). Commercial tipless silicon nitride probes (Cytosurge AG) with a 2-μm circular aperture were used. The spring constants of the probes were calibrated using the thermal tuning method, having a measured value of 0.3 and 2.5 N/m. The deflection sensitivity was also carefully calibrated by averaging the slopes of deflection versus voltage of four forward force spectra measured on glass in PBS (Thermofisher, USA) before each experiment. A fluorescent polysterene 4/6 μm bead (Degradex, USA) was fixed with negative 800 mbar pressure underneath the tipless probe filled with PBS.(*37*) The reversibility of changing bead underneath also ensures a clean contact with the hydrogel surfaces. The microgels were sedimented on the petri dish in PBS. Each microgel was selected optically and approached with 20 nN at 2 μm/s. The diameter of the bead is optimized for the indentation depth and indentation force. Acquired force distance curves (F, δ) were fitted using Hertzian model to extract the Young's moduli: E, assuming a spherical contact with corresponding radius: $R_{indenter}$ of the fluorescent bead, and a Poisson's ratio, ν, of 0.5.(*81*)

$$F = \frac{4}{3}\frac{E}{1-v^2}\sqrt{R_{indenter}}\;\delta^{\frac{3}{2}} \tag{S1}$$

1.2. *Compression testing*

To compare the Young's moduli, E, and determine the Poisson's ratio, ν, of our PEGNB hydrogel networks, we performed compression tests with a TA XT Plus Texture Analyzer (Texture Technologies). 5 mm hydrogel disks ($h = 1$ mm) were prepared and the force, F, vs distance, d, was measured while indenting (0.02 mm/s approaching speed) with a cylindrical flat punch (2 mm diameter). During indentation of the material, force increases linearly with displacement. Based on linear elasticity, the slope of this curve yields E via the following equations:

$$F = 2E^*R_{indenter}d \tag{S2}$$

$$\frac{1}{E^*} = \frac{(1-v^2)}{E} \tag{S3}$$

$$E = G/2(1+v) \tag{S4}$$

where G was determined from oscillatory rheology of bulk hydrogels.

2. Computational details and models

2.1. *Determination of microgel size distributions*

Bright-field images of microgel populations (at least 100 microgels) were taken on a glass slide using Nikon Eclipse Ts2 inverse microscope after droplet collection and subsequent cross-linking. Particle size distributions were analyzed using ImageJ software with standard built-in functions. The images were first converted to binary and thresholded according to their contrast. In cases where microgel borders were overlapping, the watershed function was used. Particle analysis function was applied to analyze each particle area, the average particle area, and the particle count. From the analysis, particle size distribution was calculated and plotted as a histogram of particle size versus frequency.

2.2. *Quantification of microgel deformations*

Microgel deformations were calculated from the obtained fluorescent images using an inverted confocal laser scanning microscope (LSM 780, Axio Observer; Zeiss) using an EC Plan-Neofluar 10x/ 0.30 Ph1 M27 objective. Each confocal image (1024 × 1024 pixel resolution, 1.384×1.384 μm pixel size) was obtained in z-stack (300 μm stack depth, 8 μm step size). Microgel packings in FITC-dextran loaded PBS were excited at a wavelength of λ= 488 nm, and the emission was detected at λ = 500–525 nm. The z-stack.czi images were exported as TIF RGB images into ImageJ and analyzed using a custom-made Macro. Briefly, an in-focus slice of microgel layer was selected, converted to binary and thresholded according to their contrast. After setting the scale, microgels in the slice were identified using particle analysis function. Using particle centers, circles were fitted and overlaid onto each microgel detected. Subsequently, the extent of overlap of the fitted circles were measured to estimate the extent of deformation on microgel surfaces.

2.3. *Energy dissipation*

Dynamic yielding process observed in many soft materials involve a transition from solid-like to liquid-like behavior. During oscillatory shearing, these materials exhibit an overshoot in loss moduli, G'' which is often termed as the Type III behavior.(*47*) For colloidal gels, the this effect is believed to originate from cage constraints that the particles are under the influence of.(*82*) Since Brownian motion is absent in granular scale microgels, we proposed that their repulsive contact probably play a role in the G'' overshoot.

Following the methods published earlier, loss moduli, G'', measured from strain sweep tests were normalized to their plateau values to remove the background dissipation. Normalized curves were fitted to a log-normal function using MATLAB. In cases where scattered background dissipation was observed, scattered data points were removed from the fitting function in order not to underestimate the overshoot (**Figure S15**).

$$E_d = \int G''(\gamma)\,\gamma\,d\gamma \qquad\qquad (S5)$$

Fitted curves were then integrated over the strain interval, which gave an estimation for energy dissipated per unit volume via **Equation S5**.

The dynamic moduli in strain sweep tests are cycle averaged values of energy storage and dissipation. Large-amplitude oscillatory strain (LAOS) measurements provide a time-resolved picture of the complex yielding and energy dissipation process.(*83*) In a typical elastic Lissajous-

Bowditch (LB) projection, time periodic oscillatory stress (σ) responses are plotted against the imposed strain. At low strain amplitudes, elastic LB projections are ellipses, indicating predominantly elastic material response. As the strain amplitude is increased, the elliptical shape of the response distorts, indicating non-linear behavior and the existence of unrecoverable energy dissipation. The energy dissipated per unit volume in a LAOS cycle can be interpreted by calculating the area enclosed by the LB curve according to **Equation S6**.

$$E_{d\,(LAOS)} = \int \sigma \, d\gamma \tag{S6}$$

As the LB curve for a perfectly plastic response is always a rectangle that encloses the measured response, perfect plastic dissipation (PPD), a dissipation ratio can be determined by normalizing the by the PPD (**Equation S7**), which allows comparison of the dissipation behavior across samples.

$$Dissipation\ ratio = \frac{E_{d\,(LAOS)}}{PPD} \tag{S7}$$

2.4. *Affine and Phantom network models*
Rubber elasticity theory explains how deforming polymer chains in a cross-linked network causes a reduction in entropy, which results in an entropic restoring force (of order RT per mole of elastically active network strands) that causes the polymer chains to return to their equilibrium state. Based on this, the number of elastically active network strands, ν, can be used to estimate the shear modulus, G, of a network through $G_{0,\,affine} = \nu RT$.(*84*) Fluctuations of the cross-links are considered in the phantom network model by deducting the total concentration of cross-links, μ, from ν, giving $G_{0,\,phantom} = (\nu-\mu)RT$.(*85*) To predict the bulk hydrogel shear moduli, we used the phantom network model. Assuming rapid step-wise kinetics of thiol-ene chemistry, we considered macromer PEGNB cross-linking with full reaction efficiency, p=1. From the ^{1}H NMR measurement, we determined the functionality of the 8-arm PEG-NB polymer to be f=6. Accordingly, we find μ = [M] and ν = 3[M], where [M] represents the polymer concentration. Therefore, the shear moduli can be written as **Equation S8**.

$$G_{0,phantom} = 2[M]RT \tag{S8}$$

Figure S2 shows the scaling of shear modulus of PEG-NB bulk hydrogel networks as a function of polymer content predicted according to Affine and Phantom network models. The measured shear moduli of bulk hydrogels (indicated in blue) were lower compared to the estimated values possibly due to network defects.

2.5. *Hertzian contact*
We hypothesized that in the LVE region, the macroscopic stress in the material originated primarily from the normal component of the contact forces. This was based on the assumption that the contacts were pairwise and the asperities (surface roughness) were much smaller than the size of the particles, thanks to the microfluidic templating method that gives rise to highly spherical particles. The solution of the Hertz contact problem is therefore a reasonable representation of

pairwise contacts for granular hydrogels in the LVE region as the model assumes small amplitudes of strain. According to Hertzian elastic contact, the normal force, F_N, dictates the indentation depth, δ, of the contacting particles of radius R_0 and depends on the contact modulus, E^* of the pair.(55) We calculated microgel deformations using the Hertzian contact model that provides a relationship between applied force and material deformation according to **Equation S9**.

$$F_N = \frac{4}{3} E^* \delta^{3/2} (R^*)^{1/2} \tag{S9}$$

We considered that the microfluidic production result in low dispersity ($R_{p,1} \approx R_{p,2} = R_0$) and each microgel is chemically identical ($E_{p,1} \approx E_{p,2} = E$). Therefore, E^* and R^* can be calculated via **Equation S10** and **S11** respectively, where $\upsilon_{p,1}$ and $\upsilon_{p,2}$, and $E_{p,1}$ and $E_{p,2}$ represent the Poisson's ratio and the Young's modulus of the interacting microgels respectively.

$$\frac{1}{E^*} = \frac{(1 - \upsilon_{p,1}^2)}{E_{p,1}} + \frac{(1 - \upsilon_{p,2}^2)}{E_{p,2}} \approx \frac{2(1 - \upsilon^2)}{E} \approx \frac{1}{2G_0} \tag{S10}$$

$$\frac{1}{R^*} = \frac{1}{R_{p,1}} + \frac{1}{R_{p,2}} \approx \frac{2}{R_0} \tag{S11}$$

Therefore, for two body elastic contact the equation can be expressed according to **Equation S12**.

$$F_N = \frac{4}{9} E \delta^{3/2} (2R_0)^{1/2} \tag{S12}$$

Direct measurements of G_0 via atomic force microscopy nanoindentation methods is possible, however with the aim of developing a simple descriptive model, we assumed that the microgel modulus was the same as the bulk shear modulus, $G_{0,bulk}$ measured using shear rheometry or estimated using the Phantom network model, $G_{0,phantom}$ (**Figure S2**).

$$V(r) = \frac{16}{45} \left(\frac{R_0}{2}\right)^{1/2} \delta^{5/2} E \tag{S13}$$

Particle deformations upon jamming give rise to strong repulsive interactions, acting perpendicularly to the contacting facets. It was shown that for granular-scale particles, around random close packing the internal polymer concentration doesn't change and no osmotic resistance is measured upon contact, unlike colloidal particles.(86) Therefore, the repulsive potential is an appropriate way to represent the interactions between microgels, as represented in **Equation S13**. Particle deformations give rise to strong repulsive interactions. The broad implication of Hertzian contact on the granular hydrogels is that *V(r)* is zero for microgels that are not in contact and increases dramatically with increasing particle deformation.

2.6. *Estimation of contact forces*
In order to estimate the microgel deformations created in the hydrogel packings through Hertzian contact model, knowledge of the contact force is necessary. Force distribution is a consequence of

the applied load on the granular hydrogels, which leads to finite effective forces on each particle pair. As exact measurement of microgel contact force, F_N in a packing is not possible, we set out to determine lower and upper bounds that allowed us to approximate the order of magnitude F_N upon contact. Accordingly, we started with the total applied force, F and implemented a mean-field approach to force distribution. The force transducer of the rheometer recorded values of $F = 0.01$ N during oscillatory shear measurements, whereas the gravitational force on the granular hydrogel packing is approximately $F = 0.005$ N, considering the weight of the hydrogel packing of the geometry (as the packing is able to hold its weight without any external load) according to **Equation S14**

$$V = \pi \, r_{plate}^2 \, h \qquad (S14)$$

where $r_{plate} = 8$ mm determined by the measuring plate and $h = 1$mm set by the z-stage of the rheometer.

According to this geometry, we determined an estimate of the number of microgel layers and number of microgels in each layer. With this logic, the number of microgels in each layer equally share the total force F, and each microgel column transmits the force perpendicular to the Peltier plate. Consequently, we forecasted a lower bound of $F_N = 0.02$ μN and an upper bound of $F_N = 0.4$ μN per microgel contact for microgels of size Ø = 55 μm. The average F_N was fixed in all packings comprising identical microgel size, since the packing fraction under the centrifugal jamming conditions is unaffected by microgel stiffness. However, for packings of different microgel sizes will result in different F_N. The scaling for F_N was calculated again according to an approximation of the vertical load bearing columns that consist of microgel surfaces in the packing. The number density of microgels will vary as fewer microgels of larger size can be packed into the measuring geometry. Thus, F_N is inversely proportional to the number of load bearing columns and the square of microgel diameter, $(2R_0)^2$. Ultimately, we estimated that the larger microgels have higher F_N associated to the pairwise contacts **Figure S24**.

2.7. *Random close packing generation for microgels*

The determinant of mechanical stability in dense suspensions is the presence of sufficiently high number of contacts, defined by the isostatic number, z_{iso}, above which the packing does not allow collective particle motions.(*22,87*) Spatial arrangement of a random packing of hard spheres can be described in distinct volume fractions, φ. Packing limits such as random loose packing ($\varphi = 0.60$) and random close packing ($\varphi = 0.64$) exist since the spheres cannot be compressed.(*88*) Conversely, such limits are difficult to obtain for soft elastic spheres as their contacts will give rise to less steep interaction potential, $V(r)$, and particles can be deformed to large extents. Indeed, studies on compressed colloidal suspensions showed that φ values above φ_{RCP} can be achieved via mechanical or osmotic compression.(*89*) As a result, flat facets can be formed due to dramatically increased deformations on the particle surfaces.

In order to represent the contact landscape of the microgel packings, we considered a random close packing of hard spheres that can later be modified to account for the microgel deformations. Such packings can be computationally generated for both monodisperse and polydisperse systems via Lubachevsky–Stillinger and force-biased algorithms.(*64,65*) We used an open source program, based on the work of Baranau *et al.* that implements a force-biased algorithm and using particle velocities and fast compression rates to simulate closely jammed configurations and determine corresponding densities.(*90*) We calculated the number of

microgels, *n* of each size in the packings according to **Table S5**
Table S5. by accounting for the tigher random close packing compared to simple cubic ordering of the microgel**s**. Here, for the ease of simulation, particle diameters were kept as unity ($d = 1$) and the spatial coordinates of the sample were changed such that the ratio between and the volume of the particles, $V_{particle}$ and the box volume, V_{box} (described in **Equation S15**) was maintained.

$$V_{box} = x\,y\,z \tag{S15}$$

With *n* and V_{box} as input parameters, packings of different building block sizes were generated that resulted in the expected $\varphi = 0.64$. We noted that there is a slight deviation of V_{box} from the real volume, V, which is a cylinder.

$$g(r) = \frac{V_{box}}{4\pi r^2 n^2}\,R(r) \tag{S16}$$

One of the elements that can be harvested from the packing simulation is the geometrical coordinates of the particles and therefore the particle count at each location, *R(r)*. This particle count can be represented in the form of radial distribution function, *g(r)*, which describes the probability density of finding a particle at a distance *r* from the reference particle (**Equation S16**). For hard sphere packings, the pair probability strongly peaks at the radial separation *r* which is twice the particle radius $2R_0$. Likewise in the generated random close sphere packing, particles are in point contact, which corresponds to a large peak at exactly two-particle radii distance with no peak spread $2R_0 = r$. The peak of *g(r)* is independent of the average particle size and only dependent on the microstructure, therefore the packing was post-processed by scaling the radial distances to particle size range while storing the correct particle coordinates. Therefore, δ can be conveniently expressed according to **Equation S17**. As the packing characteristics were independent of microgel size and were generated in dimensionless units, we returned the obtained numbers to micron scale coordinates.

$$\delta = 2R_0 - r \tag{S17}$$

2.8. *Zwanzig and Mountain model*
A condensed system of monoatomic fluids shows an elastic response to applied mechanical force. Zwanzig and Mountain provided a statistical mechanic approach and presented a general expression for this elastic response.(*66*) The expression implements the reduction of the frequency dependent shear modulus, G_∞, into a two-body form via

$$G_\infty = nk_bT + \frac{2\pi}{15}\,N^2 \int_0^{2R_0} g(r)\,\frac{d}{dr}\left\{r^4\left[\frac{dV(r)}{dr}\right]\right\}dr \tag{S18}$$

where *N* is the particle number density (*n/V*), k_b, the Boltzmann constant, *T* the absolute temperature, *g(r)* the radial distribution function with *r* the center separation, and *V(r)* is the pair interaction potential. As the model assumes spatial isotropy, *V(r)* is strictly central for all interacting pairs. Hence, by integrating the pair interaction over radial distances and considering the number of interactions per volume, the macro-scale elastic modulus is elucidated (**Equation S18**).

Originally, the model was developed to relate the macro-scale response to the interparticle interactions when $V(r)$ has the Lennard-Jones (LJ) form. Later, Elliott and Russel showed the applicability of the expression to dense colloidal systems with repulsive Hertz potentials.(91) For systems that have LJ type potential, direct contact between the pairs is not necessary to have a non-zero contribution to the elasticity. However, for Hertz type potentials, it is implicit in **Equation S18** that only particles that contact and deform one another contribute to the observed macro-scale modulus. Therefore, the expression considers the overlap of particles and the relative distance of particle centers. At the granular scale, the thermal contribution, k_bT, to G_∞ is negligible as Brownian motion is absent. Hence the equation is simplified into **Equation S19**.

$$G_p = \frac{2\pi}{15} N^2 \int_0^{2R_0} g(r) \frac{d}{dr} \left\{ r^4 \left[\frac{dV(r)}{dr} \right] \right\} dr \qquad (S19)$$

The model was implemented previously also to demonstrate power law behavior for the volume fraction dependence of non-colloidal suspensions.(41,67) In these studies, by assuming $g(r)$ sharply peaks and using a delta function as an approximation of the radial distribution function, explicit estimations of particle overlap was discounted. Conversely, for our granular hydrogels, we estimated that the volume fraction upon centrifugal jamming conditions is similar to the close packing of hard spheres. Therefore, it is reasonable to assume that $g(r)$ of microgels in the packing has the shape of random close packing of spheres, obtained from the LS packing generation. In addition, we treat the packing such that affine movement of microgels is induced during deformations in the linear viscoelastic region. Based on these assumptions, the inference of a non-zero G_p can be calculated using numerical integration of the expression containing the radial distribution of microgels and their pairwise interaction energies. Lastly, N was extracted from the estimated number of particles according to **Table S5**.
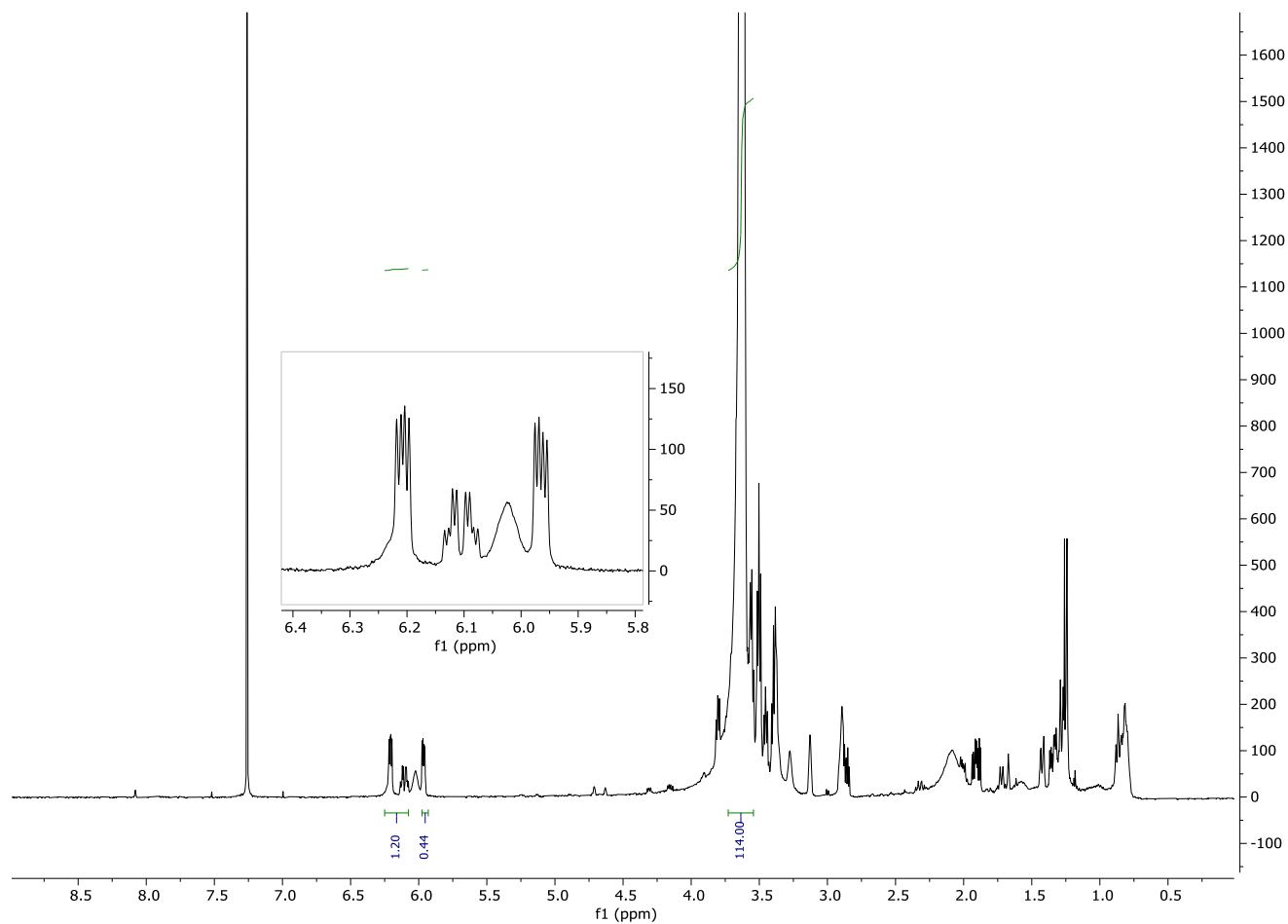
Supplementary figures

Fig. S1. ^{1}H NMR spectrum (500 MHz, CDCl$_3$) of 8-arm PEG-NB (M$_n$ = 10000 g mol^{-1}). Functionalization of the 8-arm PEG with norbornene groups was found to be 80% by calculating the relative amount of the norbornene vinyl protons (δ = 6.0–6.3, m, 1.62H) to PEG ether protons (δ = 3.5–3.9, m, 114H).
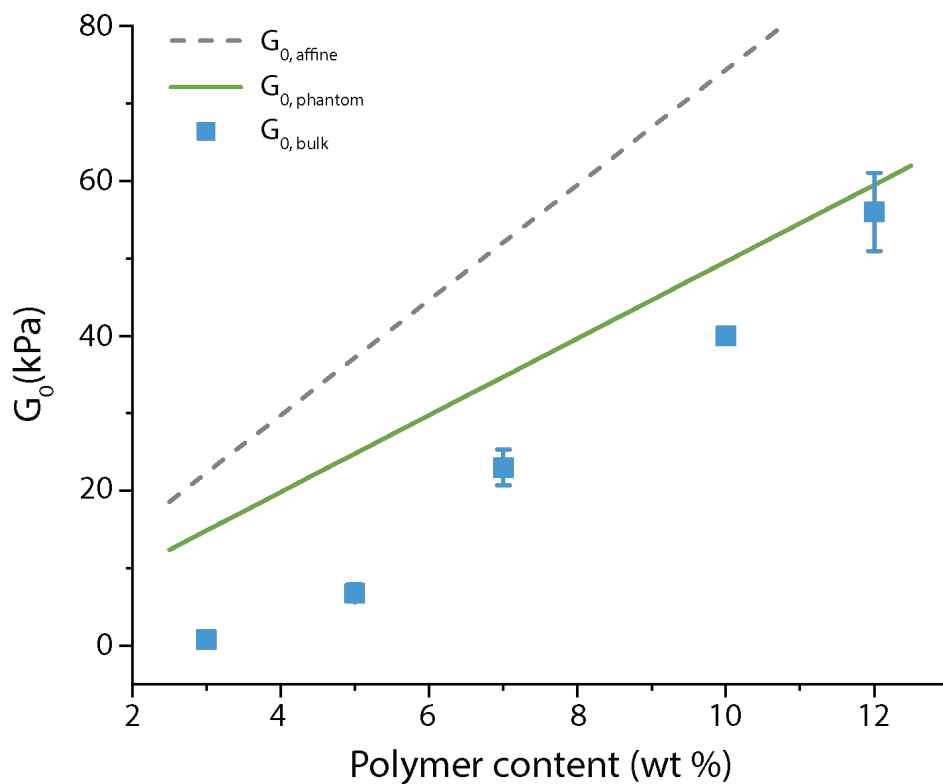
Fig. S2. Shear moduli of bulk PEG-NB hydrogel networks as a function of polymer content. Square symbols (mean ± s.d.) indicate shear moduli of bulk hydrogel disks measured via rheology while lines (continuous and dotted) represent estimated values according to Phantom and Affine network models respectively taking into account the degree of functionalization calculated from ^{1}H NMR spectrum of 8-arm PEG-NB.
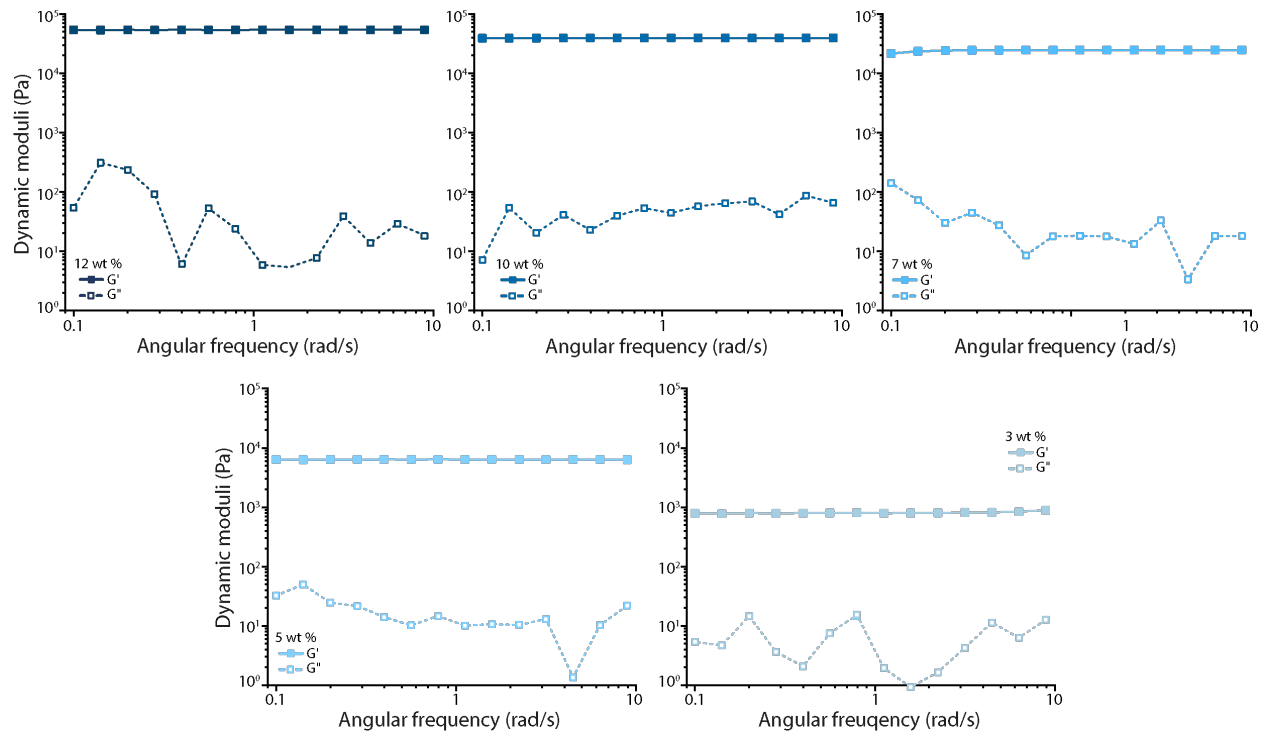
Fig. S3. Frequency dependent dynamic moduli of bulk hydrogels at varying polymer contents ($\gamma = 0.1\%$).
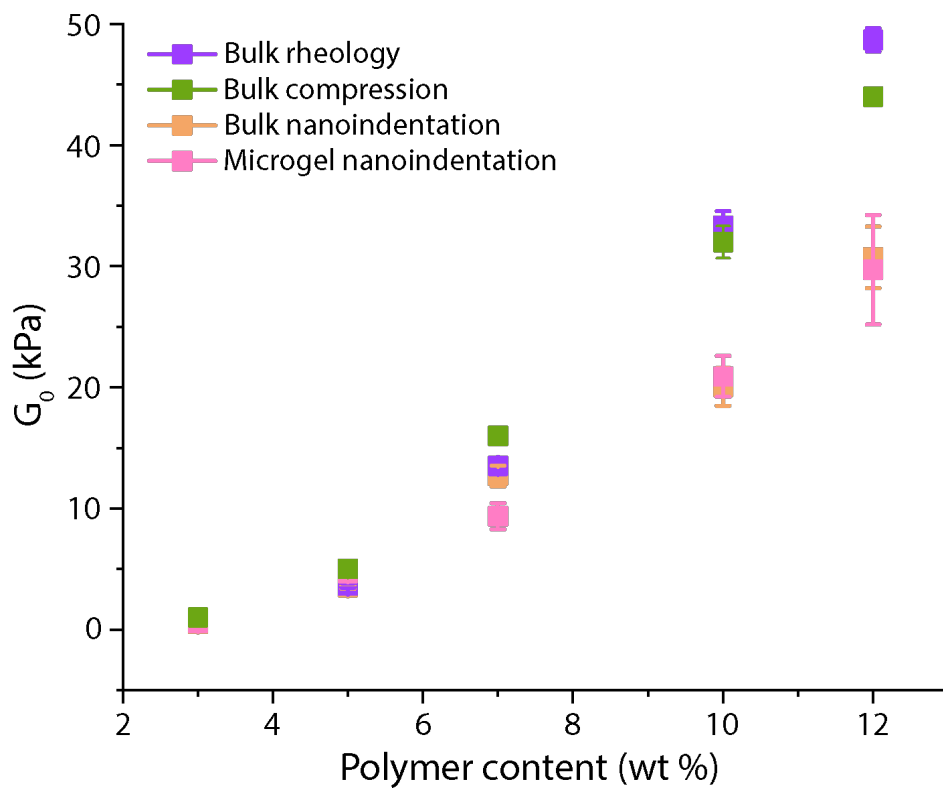
Fig. S4. Shear moduli of PEGNB hydrogels characterized via different techniques. For compression and nanoindentation tests, the extracted Young's moduli were converted to shear moduli, G_0 (assuming Poisson's ratio, $\nu = 0.5$).
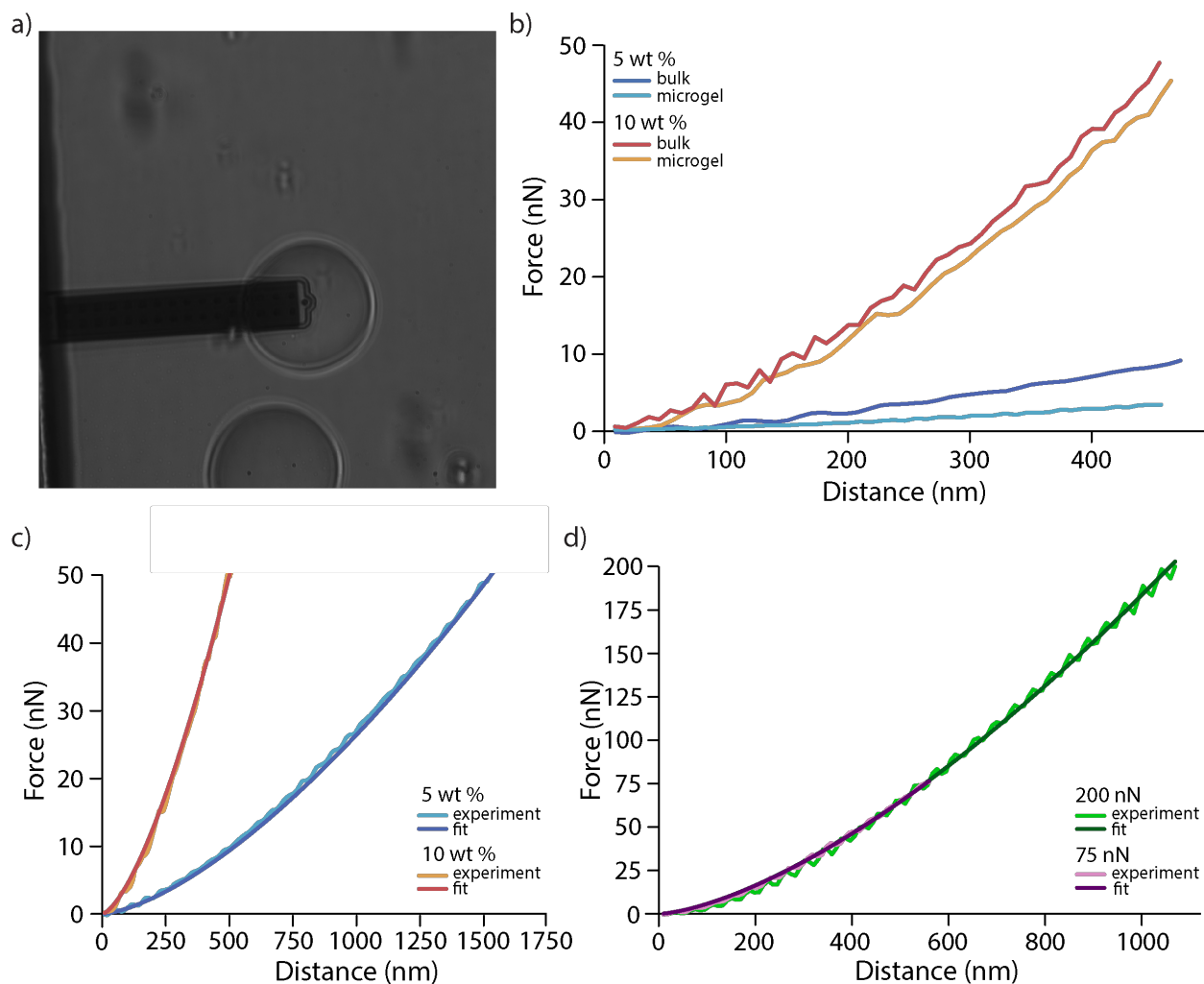
Fig. S5. Fluid force microscopy (FluidFM) tests performed on bulk and microgel samples. a) Representative image of microgel indentation with the FluidFM probe. b) Force-distance curves for bulk and microgel samples consisting of identical polymer contents, indicating the similarity in elasticity. c) Force-distance curves for microgels consisting of different polymer contents, showing the successful fitting procedure. d) Force distance curves for a microgel (10 wt%) indented at varying maximum normal forces, showing the lack of difference in indentation profile and therefore the absence of a core-shell structure. Obtained force-distance curves were fitted using the Hertzian contact model to extract Young's moduli.
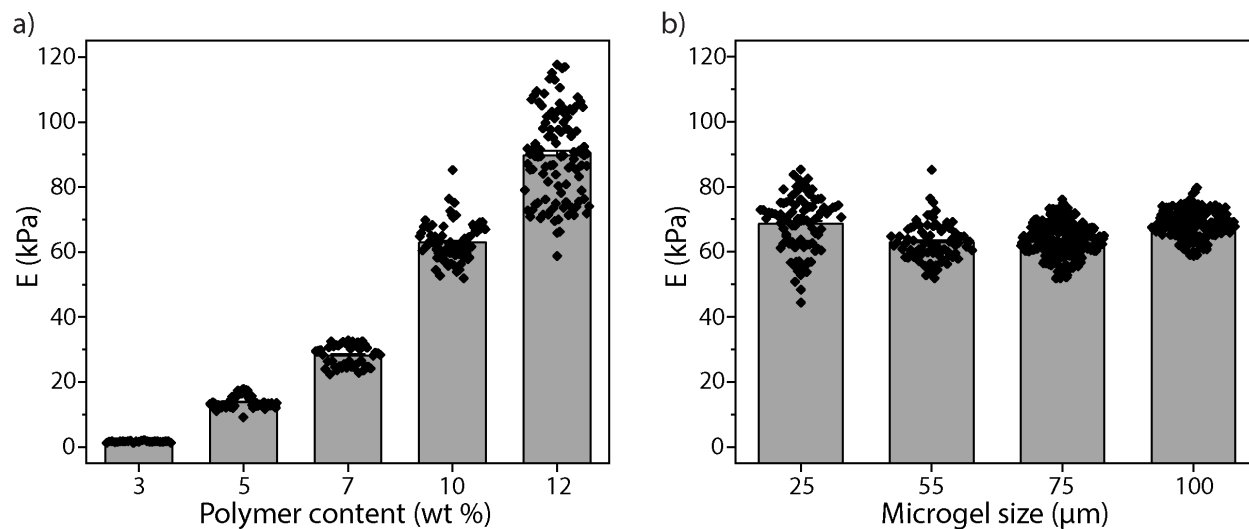
Fig. S6. Fluid force microscopy (FluidFM) tests performed on microgel samples. a) Microgels made of varying polymer contents at Ø = 55 µm. b) Microgels made of 10 wt% polymer at different sizes. Tests were done on at least n = 3 microgels with a grid of 3x3 with each point indented 3 times.
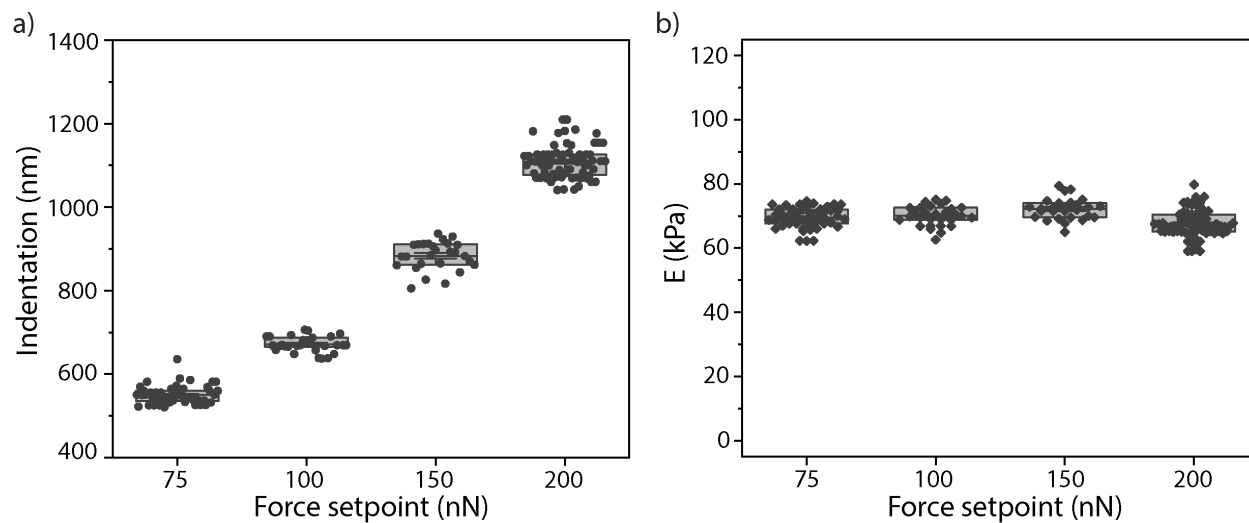
Fig. S7. Fluid force microscopy (FluidFM) tests performed on microgel samples (10 wt% polymer) probing different indentation depths. a) Indentation depths reached at different force setpoints. b) Calculated Young's moduli, E show the absence of a core-shell structure/cross-linking heterogeneity across the microgels. Tests were done on at least n = 3 microgels with a grid of 3x3 with each point indented 3 times.
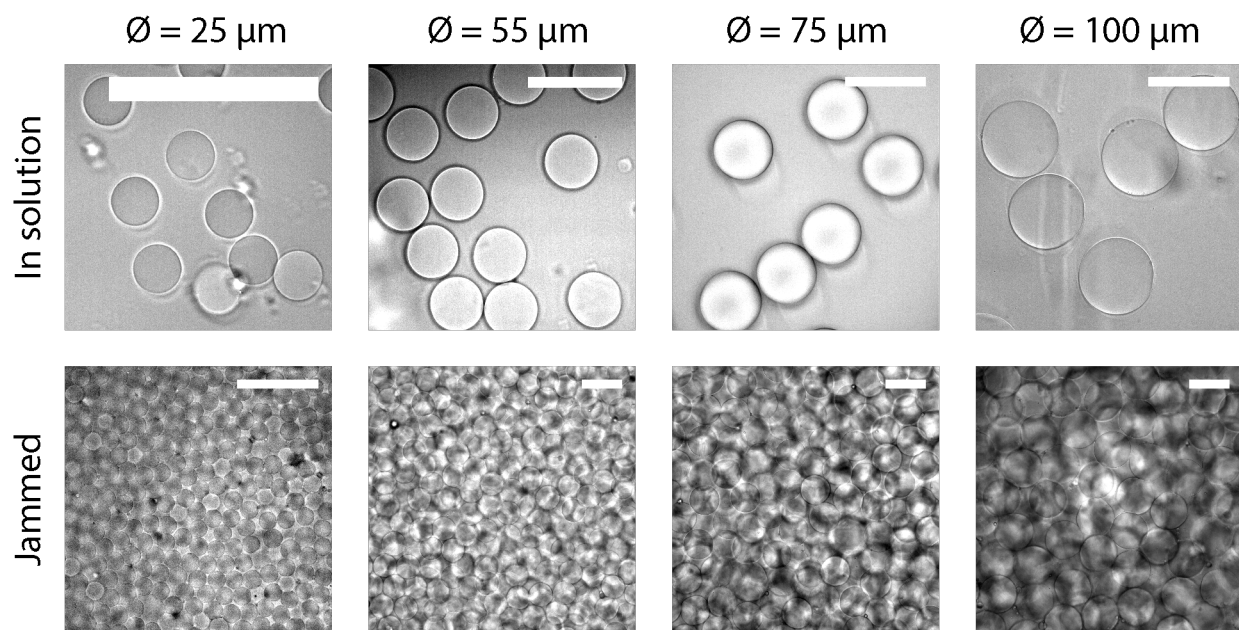
Fig. S8. Representative brightfield images of microgels (*E* = 120 kPa) in solution and jammed state. Scale bars, 100 μm.
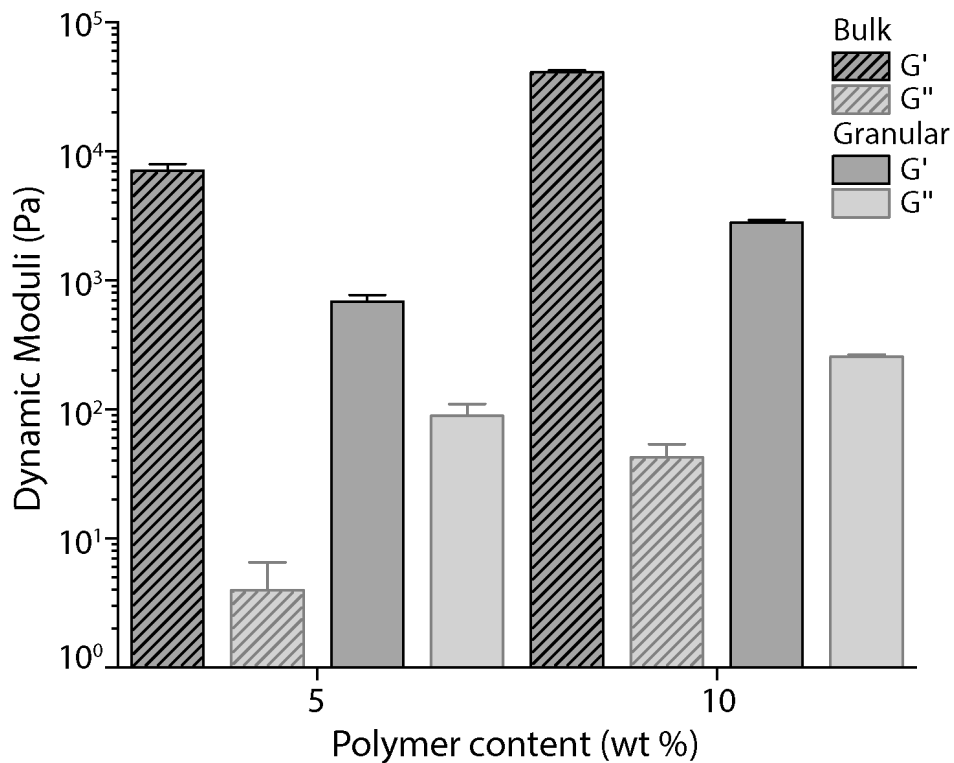
Fig. S9. Dynamic moduli of bulk and granular hydrogels of different polymer contents (Ø = 55 μm, γ = 0.1%, ω = 10 rad s⁻¹). Storage moduli of granular hydrogels decreased by an order of magnitude compared to their bulk counterparts, which was attributed to the particle nature, hence the discontinuity in the polymer network. Loss moduli increased up to two orders of magnitude possibly due to the damping effect of the packing structure.
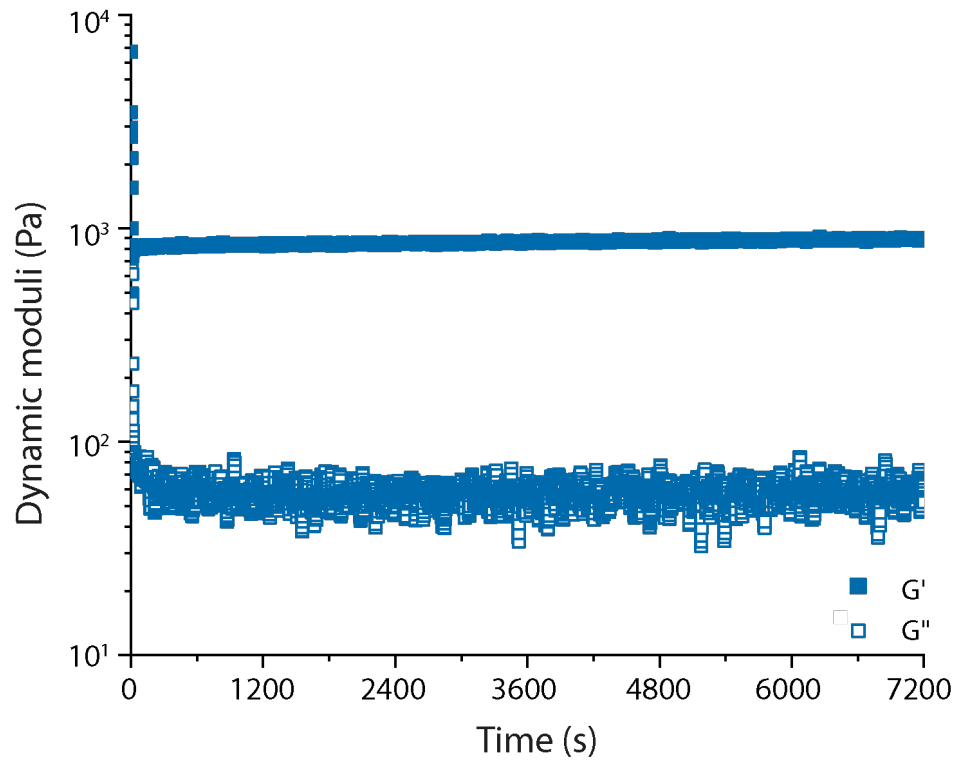
Fig. S10. Dynamic moduli of granular hydrogels (E = 20 kPa, Ø = 55 µm, γ = 0.1%, ω = 10 rad s^{-1}) over time. Storage and loss moduli of granular hydrogels remained constant for a duration of 2 hours, indicating the absence of aging and relaxation to an equilibrium.
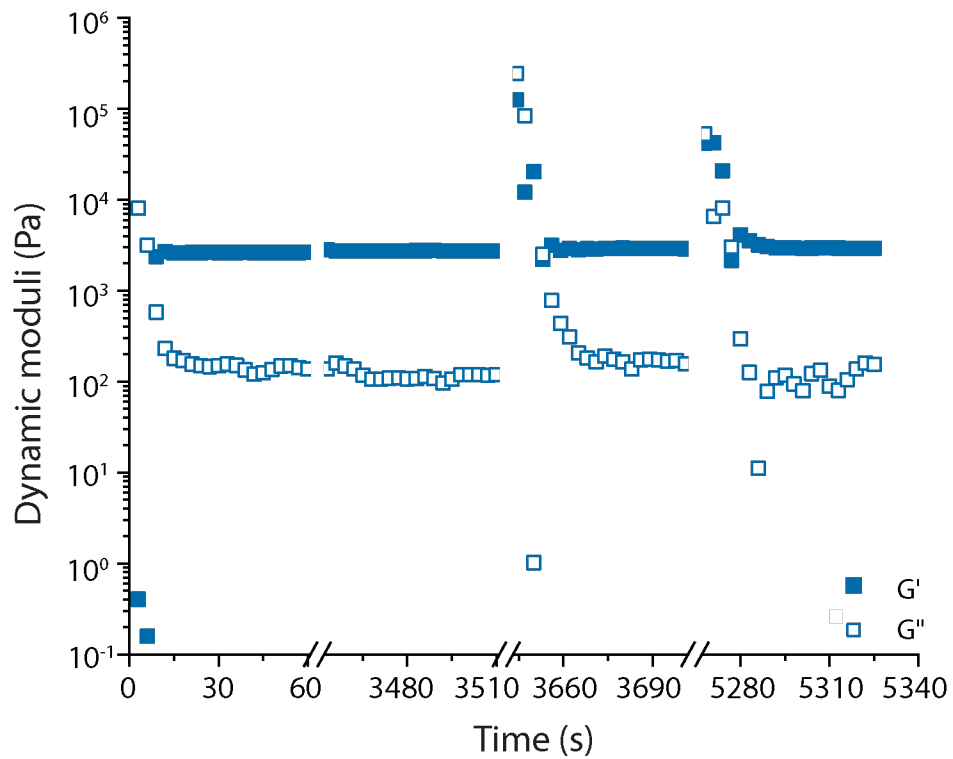
Fig. S11. Dynamic moduli of granular hydrogels (E = 120 kPa, Ø = 55 µm, γ = 0.1%, ω = 10 rad s^{-1}) in between measurement cycles. Full time-sweep trace of a measurement protocol indicating the quick establishment of properties upon pre-shear and rapid recovery of the starting storage and loss moduli between different measurements.
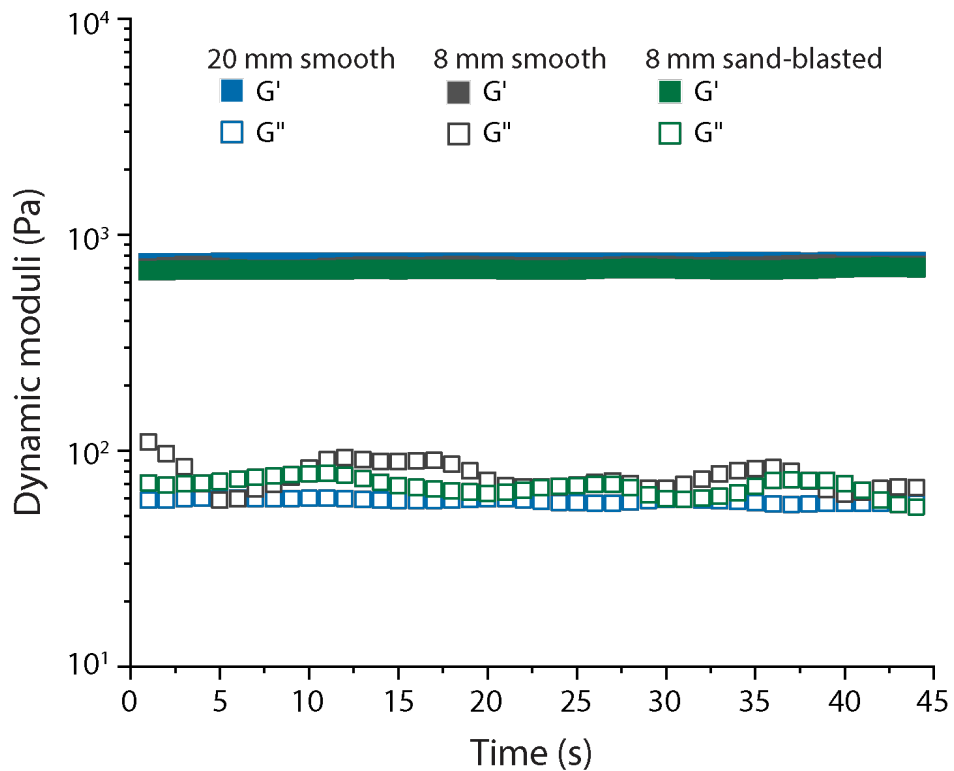
Fig. S12. Dynamic moduli of granular hydrogels (E = 20 kPa, Ø = 55 µm, γ = 0.1%, ω = 10 rad s^{-1}) using different plate geometries.

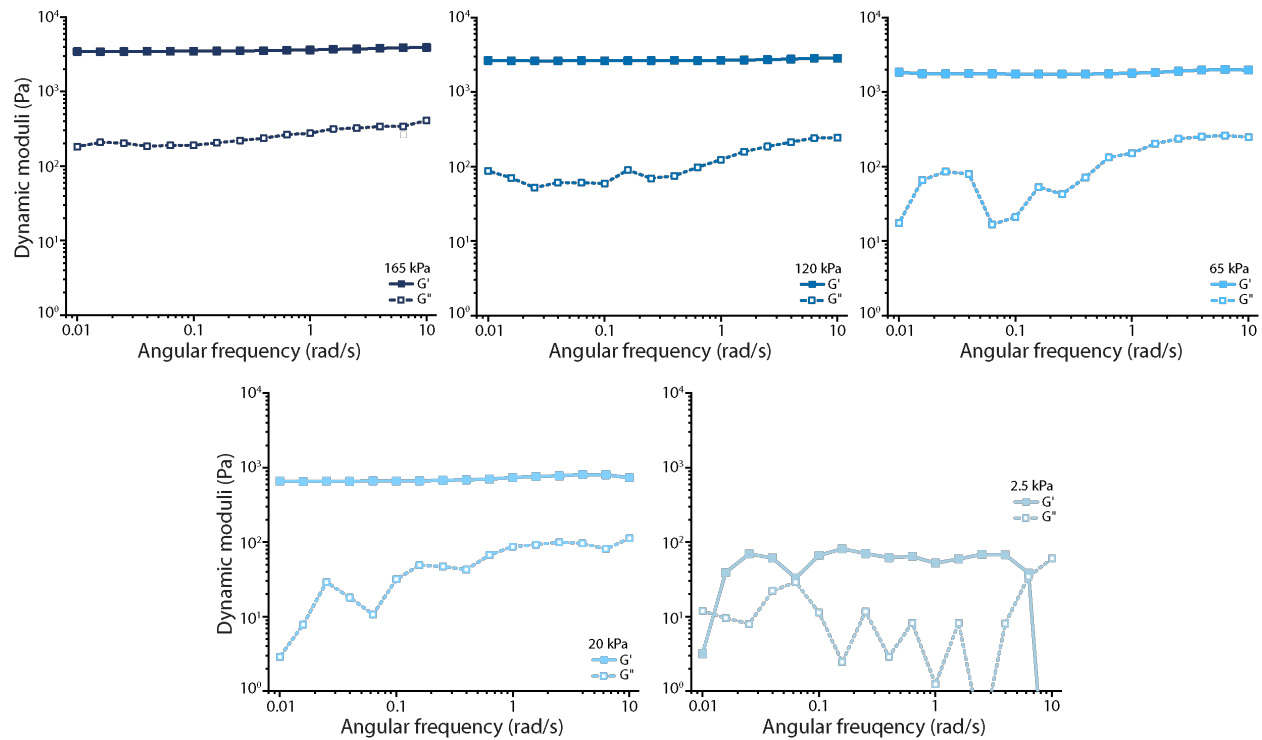**Fig. S13. Frequency dependent dynamic moduli of granular hydrogels (Ø = 55 µm, γ = 0.1%).**

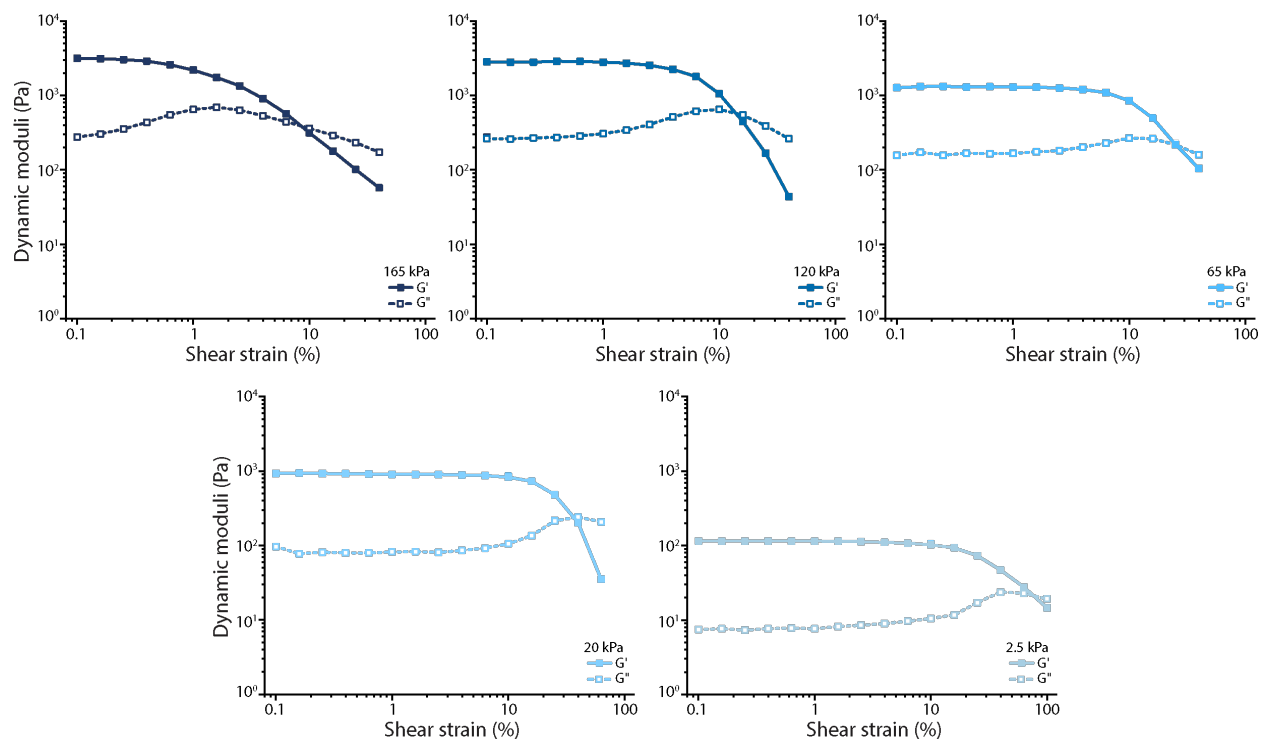**Fig. S14. Strain dependent dynamic moduli of granular hydrogels (Ø = 55 µm, ω = 10 rad s^{-1}).**
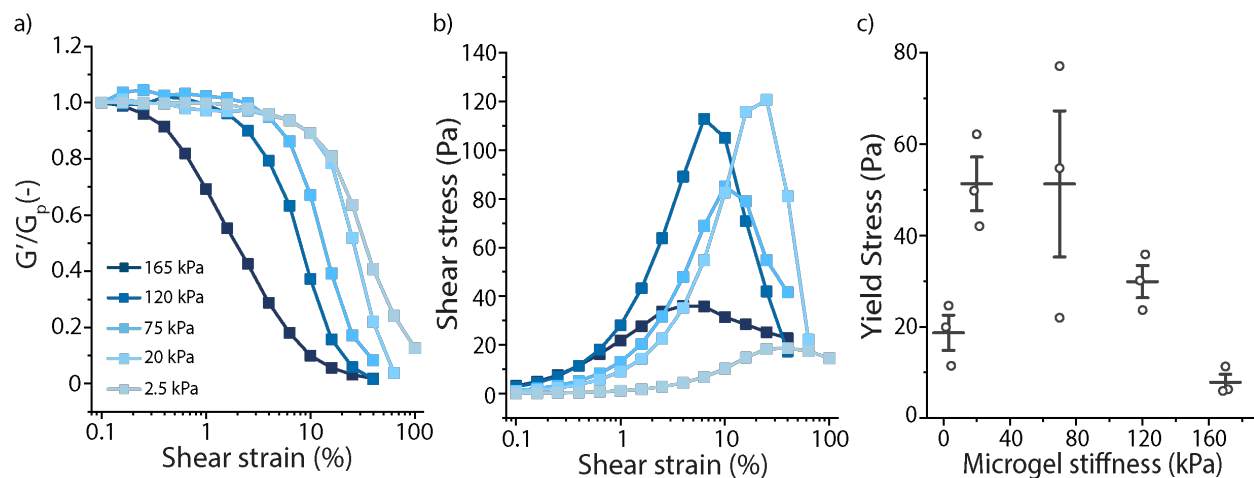
Fig. S15. Yield stress calculation for granular hydrogels from strain sweep tests (Ø = 55 µm, ω = 10 rad s⁻¹). a) Storage moduli, G', of granular hydrogels normalized to the respective plateau moduli, G_p. b) Calculated shear stress profile of granular hydrogels during strain sweep tests. c) Yield stress of granular hydrogels as a function of microgel stiffness (calculated at the point where G' fell 10% below its G_p value).
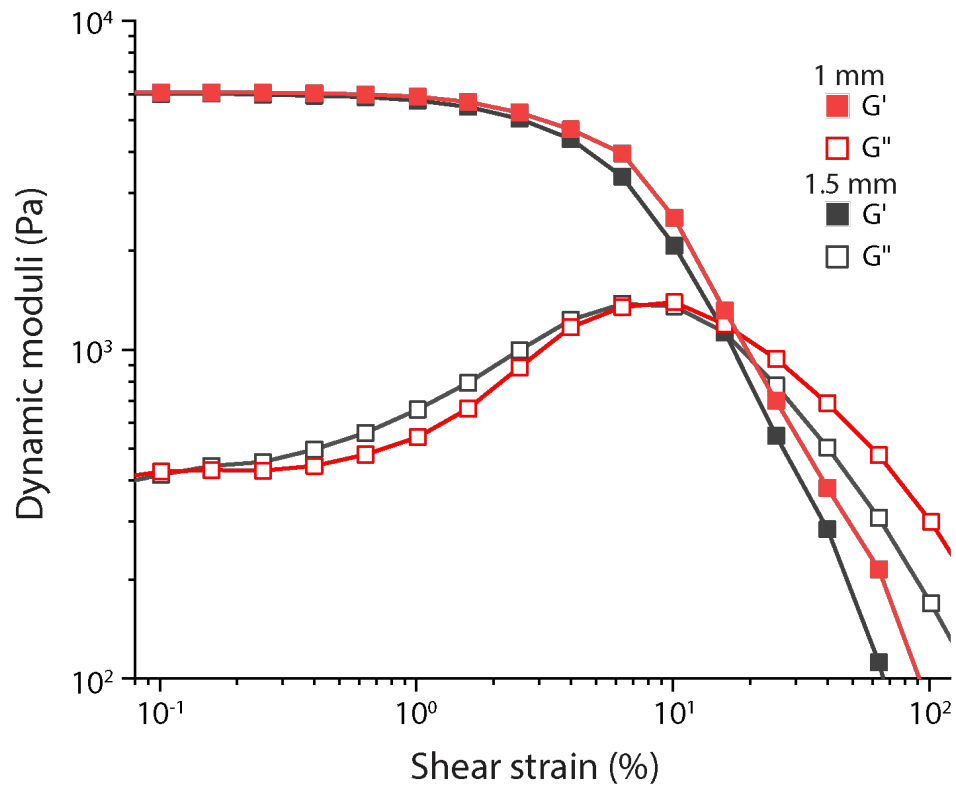
Fig. S16. Effect of measuring gap on the strain dependent rheological behavior of granular hydrogels (E = 120 kPa, Ø = 100 µm, ω = 10 rad s^{-1}).

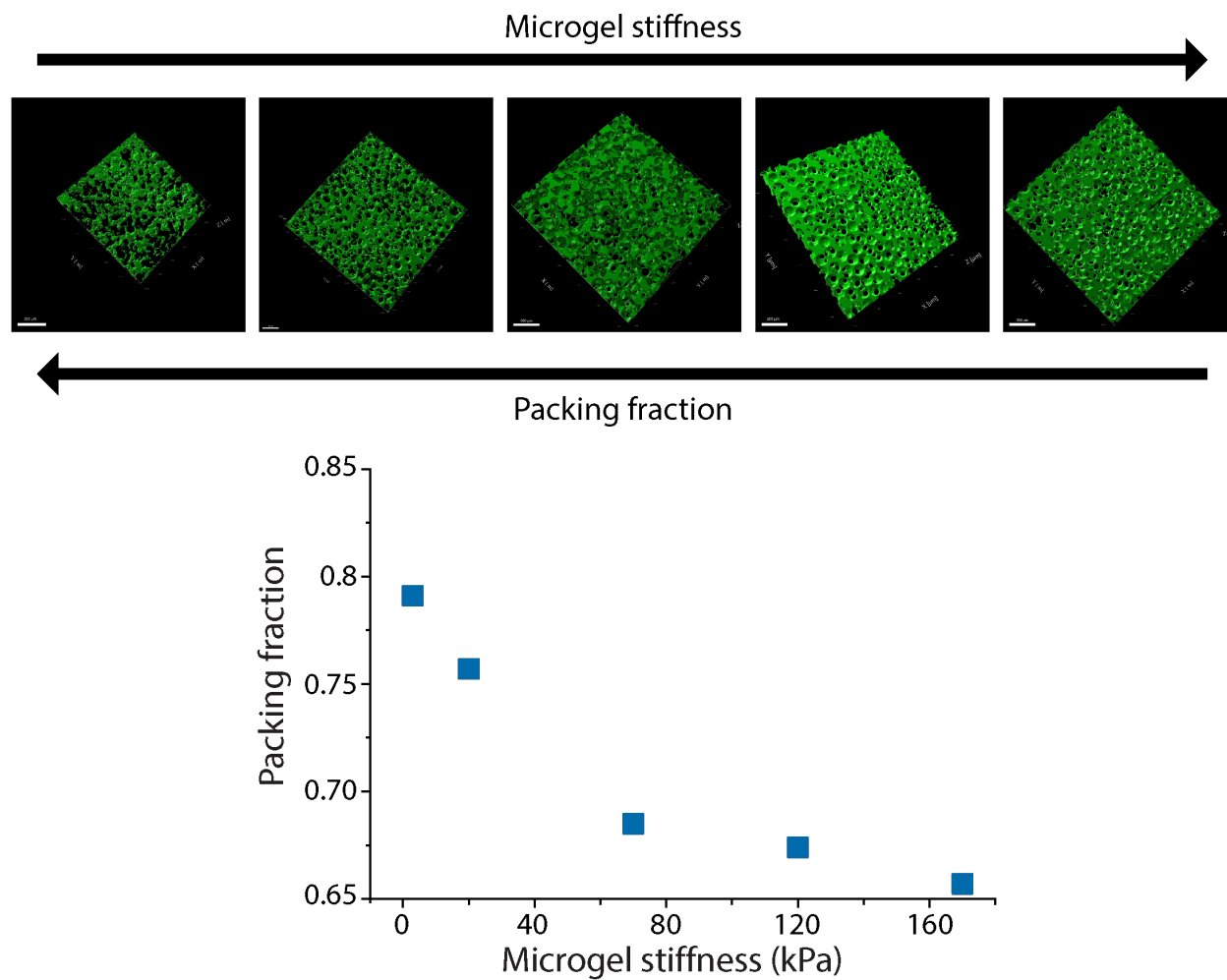**Fig. S17. Imaging analysis of microgel packings via IMARIS software.**
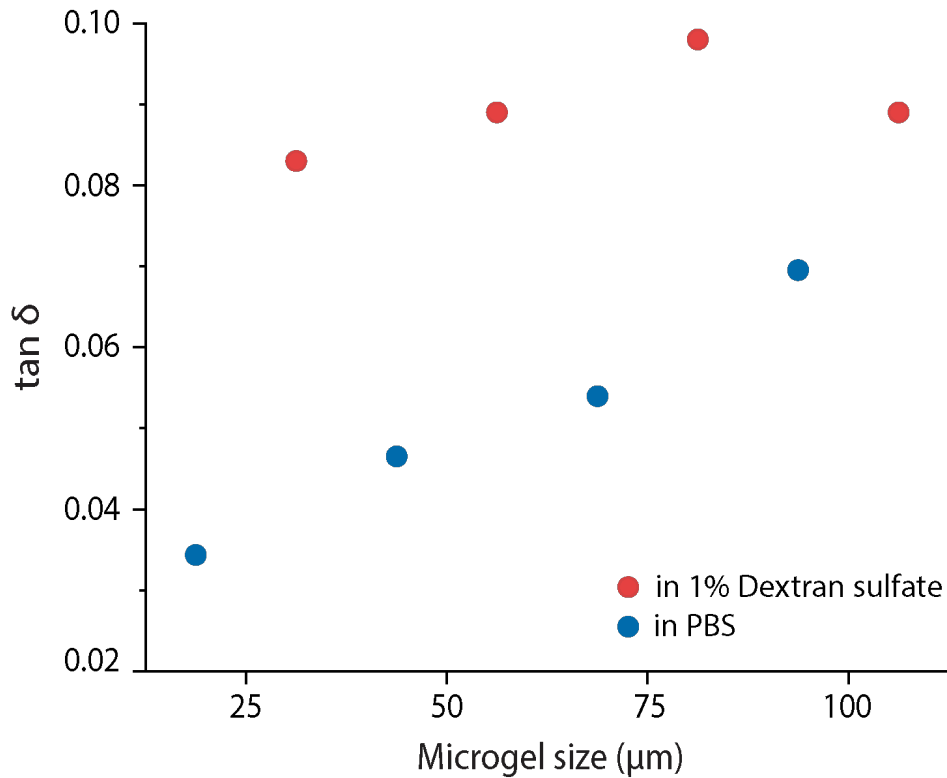
Fig. S18. Loss factor, tan δ of granular hydrogels (E = 120 kPa) jammed from a solution of PBS buffer and 1% dextran sulfate in PBS (γ = 0.1% and ω = 1 rad s^{-1}). The effect of microgel contacts in viscous dissipation of granular hydrogels were assessed by calculating tan δ in the presence of a high molecular weight polymer solution that is excluded from the microgel network. The tan δ increased in the presence of dextran solution for all microgel sizes despite the constant microgel stiffness (E = 120 kPa), indicating that the microgel polymer network is not the origin of viscous dissipation in jammed granular hydrogels.
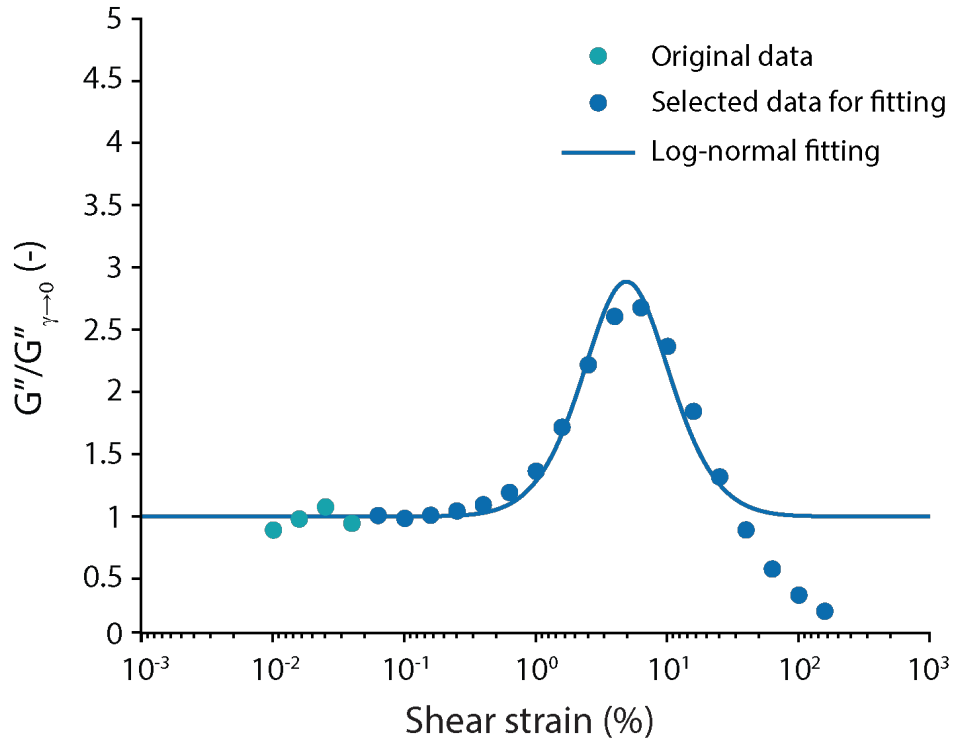
Fig. S19. Example fitting performed for the calculation of dissipated energy per unit volume, E_d of granular hydrogels. The overshoot in loss moduli obtained from strain sweep measurements were normalized by their linear response value at low shear strain ($\omega = 10$ rad s^{-1}). $G''/G''_{\gamma \to 0}$, were fitted to a log-normal distribution on MATLAB.
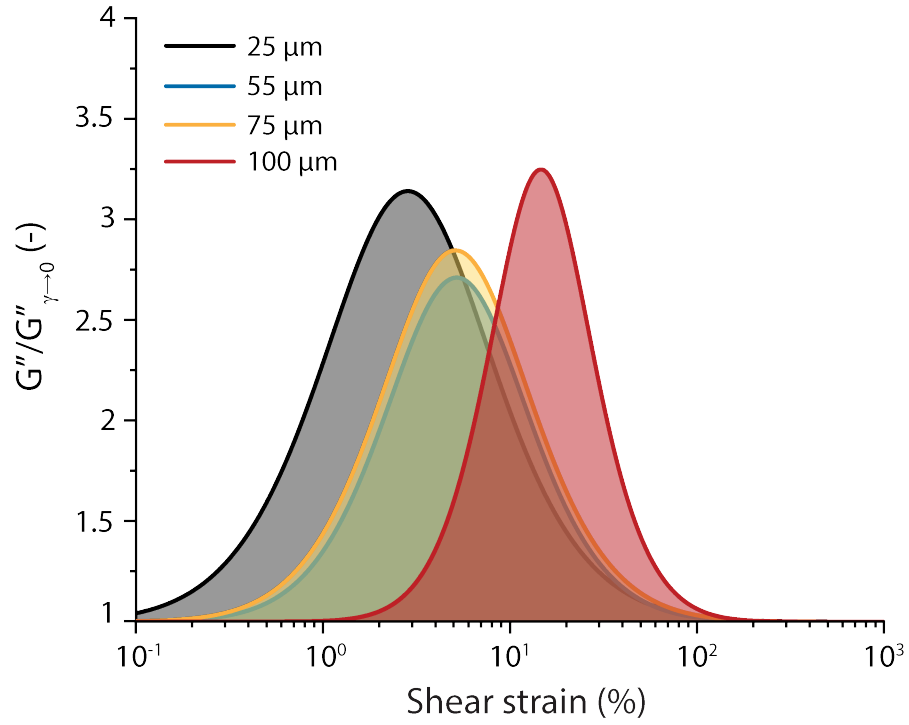
Fig. S20. Log-normal fitted $G''/G''_{\gamma \to 0}$, curves of granular hydrogels of varying building block sizes at constant stiffness (E = 120 kPa), from left to right: Ø = 25 µm, gray; Ø = 75 µm, yellow; Ø = 55 µm, blue; Ø = 100 µm, red.
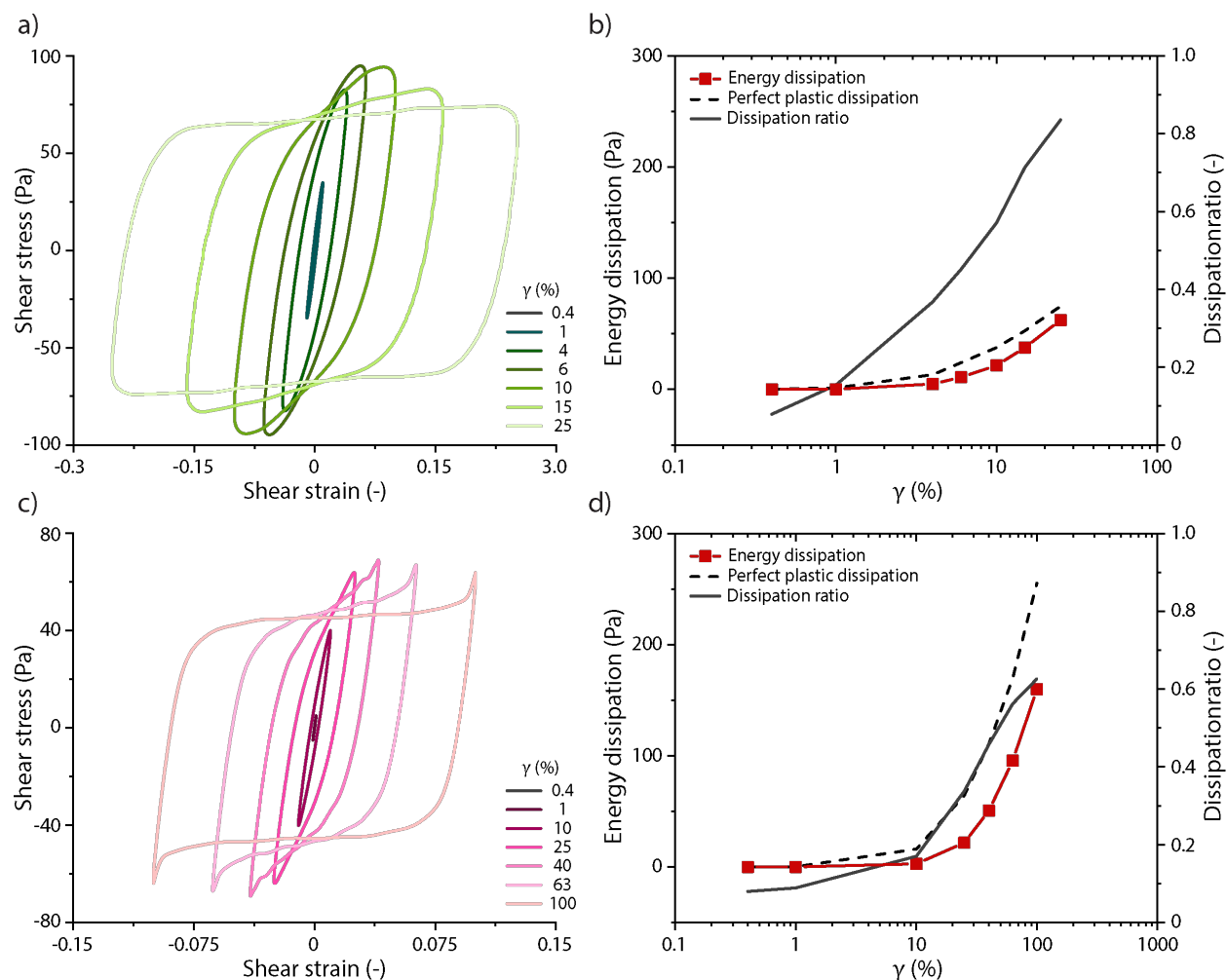
Fig. S21. Large amplitude oscillatory strain (LAOS) measurements of granular hydrogels of stiff (E = 120 kPa, Ø = 75 μm) and soft (E = 20 kPa, Ø = 75 μm) building blocks at ω = 1 rad s^{-1}. Elastic Lissajous-Bowditch (LB) projections of a a) stiff (E = 120 kPa) and c) soft (E = 20 kPa) microgel packing plotted as stress versus oscillatory strain. The cycles selected for strain amplitudes show progressive changes in the stress response. Energy dissipation per unit volume for b) stiff (E = 120 kPa) and d) soft (E = 20 kPa) microgel packings as well as perfect plastic response were calculated for each cycle of strain amplitude. Comparison via dissipation ratios show that soft microgel packings show higher plastic response during yielding.
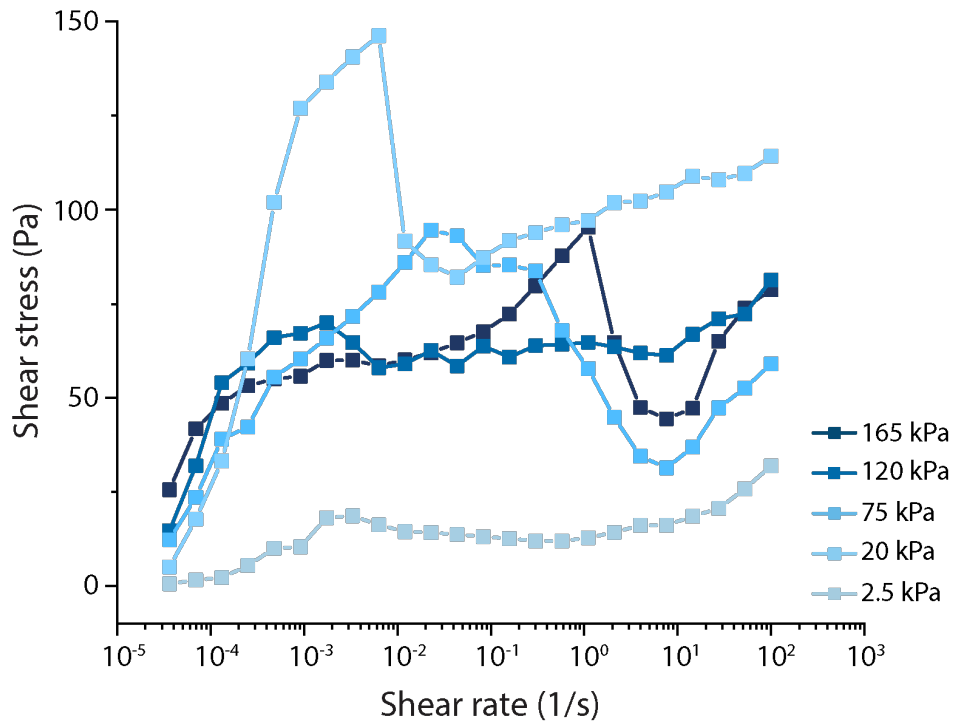
Fig. S22. Shear stress of jammed granular hydrogels (Ø = 55 μm) of varying stiffness of building blocks as a function of shear rate. The steady increase in shear stress at low shear rates indicated reliable measurements. At increased shear rates the samples exhibited characteristics of slip and shear banding.
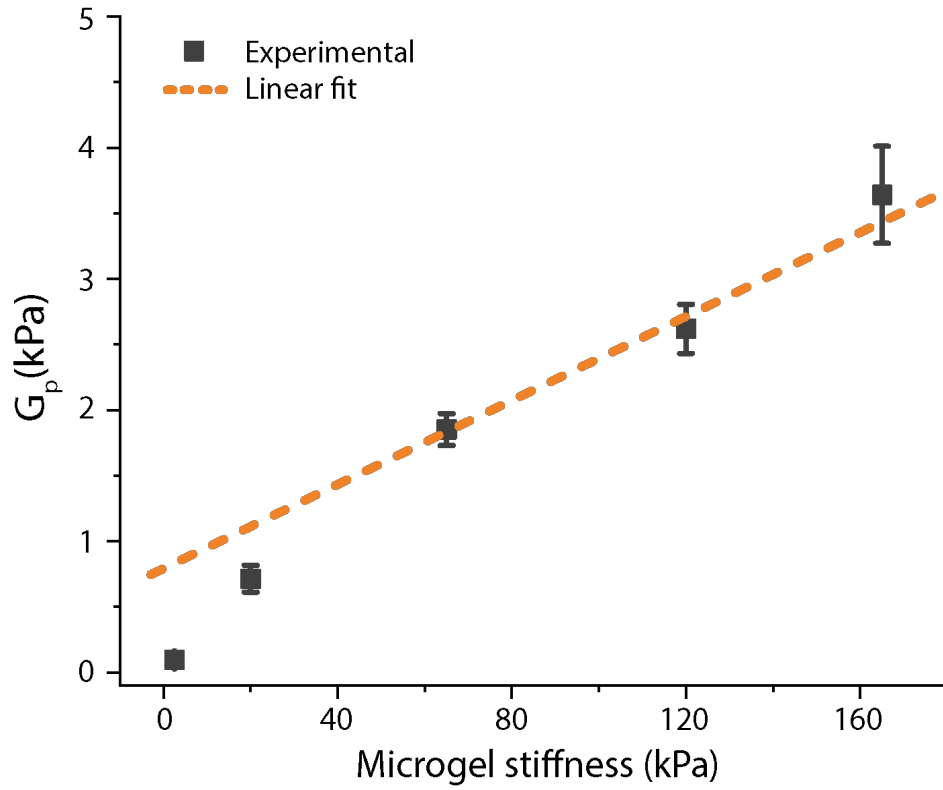
Fig. S23. Hard sphere (HS) model fitting of Plateau moduli, G_p, of stiff (E = 65, 120, 165 kPa) microgel packings.
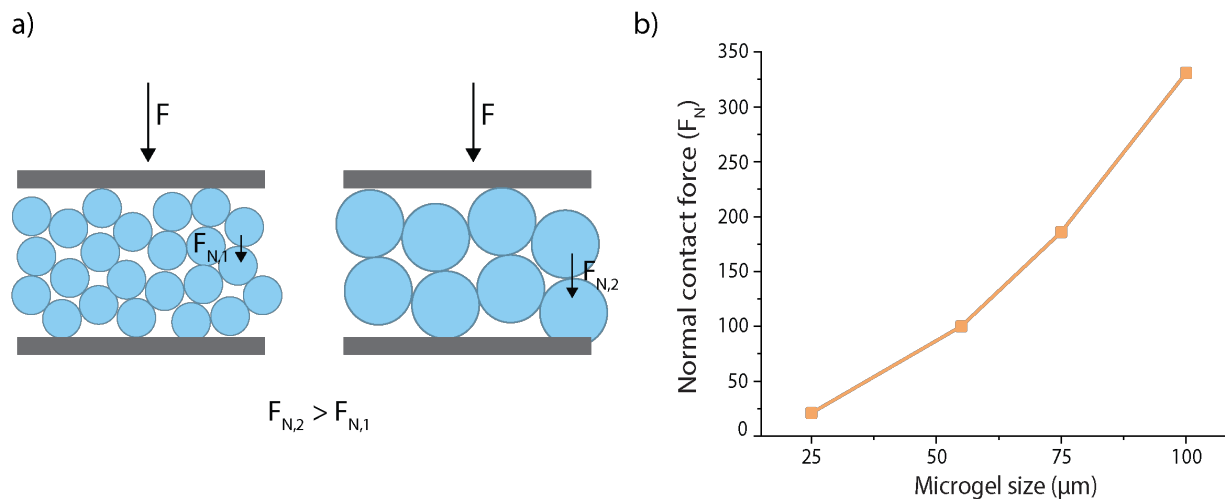
Fig. S24. Force scaling estimated for granular hydrogels of varying building block sizes. a) The scaling was calculated according to an approximation of the vertical load bearing columns that consist of microgel surfaces in the packing (where z-stage of the rheometer is fixed to 1 mm gap). b) The contact force F_N (in nN) is inversely proportional to the number of load bearing columns and the square of microgel diameter, $(2R_0)^2$.
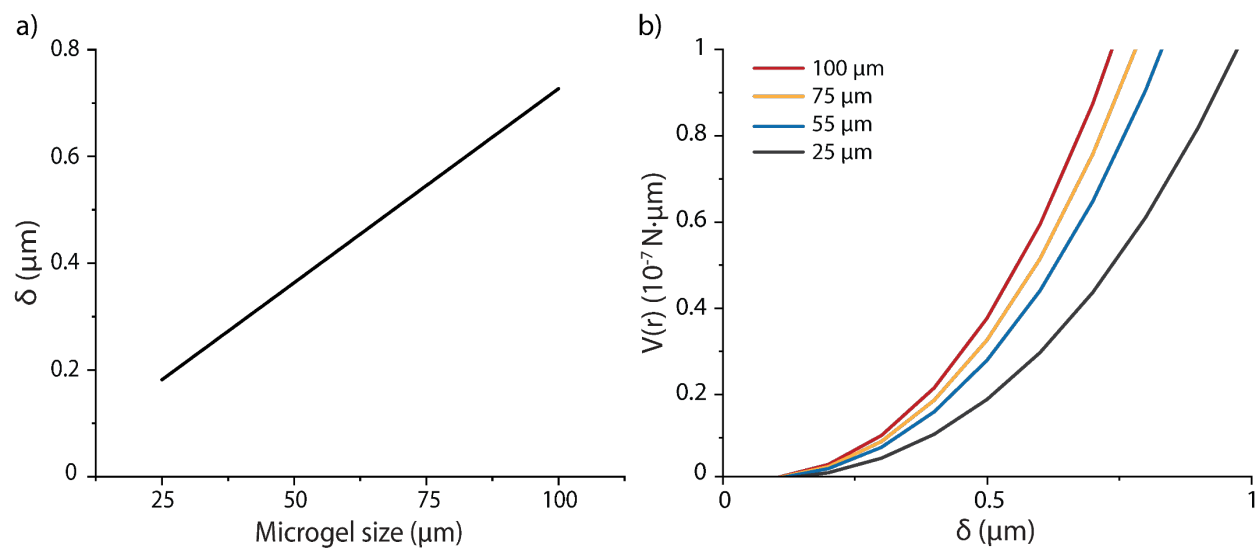
Fig. S25. Hertzian contact estimated upon microgel contact for varying building block sizes at constant microgel stiffness (E=120 kPa). a) Indentation depth, δ, calculated according to the contact force scaling estimated that larger microgels form result in higher surface deformations upon contact. b) The resulting repulsive potential, $V(r)$ increases as a function of microgel size, from left to right: $\varnothing$ = 100 μm, red; $\varnothing$ = 75 μm, yellow; $\varnothing$ = 55 μm, blue; $\varnothing$ = 25 μm, gray.
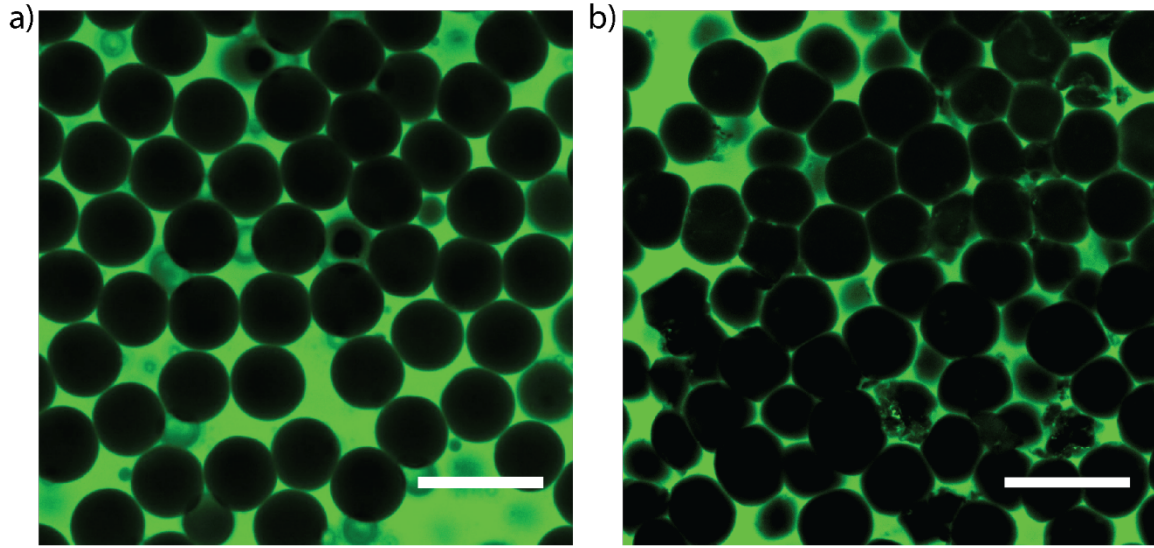
Fig. S26. Confocal imaging of granular hydrogels. Z-stack slices of a) stiff (E = 120 kPa, Ø = 55 μm) and b) soft (E = 20 kPa, Ø = 55 μm) microgel packings. Scale bar, 100 μm.
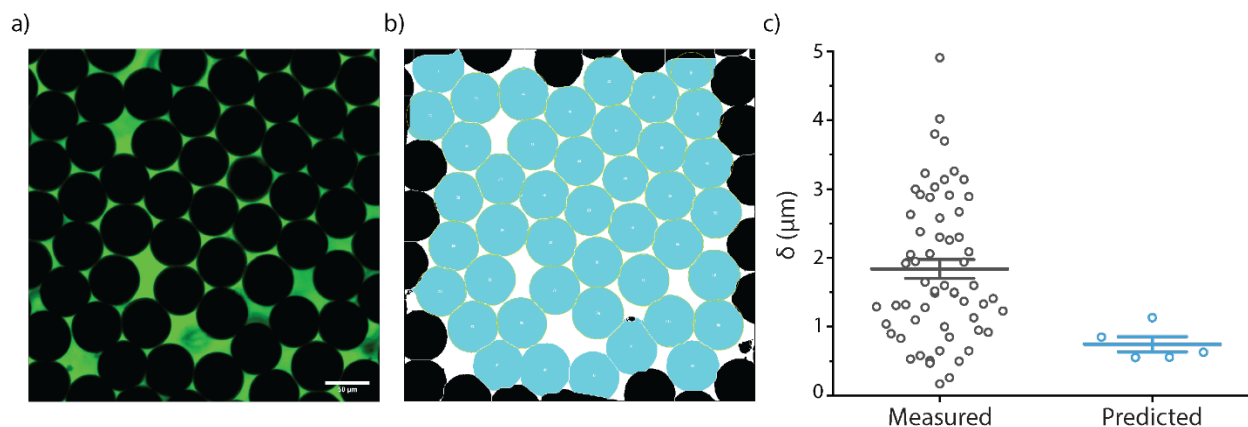
Fig. S27. Microgel deformations measured from confocal z-stack images. a) Confocal z-stack slice of granular hydrogels made of E = 120 kPa, $Ø$ = 55µm building blocks. b) Microgels were identified using custom ImageJ Macro and circles of average microgel size were fitted to determine the extent of indentation. Indentation depth (δ) for each microgel pair was measured via measuring the overlap of the fitted circles. c) Indentation depth (δ) measured from the confocal slice compared with the predicted values from the contact model.

Supplementary tables

Microgel diameter (µm)	Oil (µL/min)	PEG (µL/min)
25*	10	1
55	10	1
75	10	4
100	10	10

Table S1. Relative flow rates of oil and hydrogel precursor solutions in the microfluidic chip that give rise to defined microgel sizes. For size Ø = 25 µm, a flow-focusing device with smaller dimensions was used in order to increase throughput.

Time (s)	Measuring gap (mm)	Normal force (mN) 120 kPa	20 kPa
3	1	14.65	33.44
6	1	14.64	32.8
9	1	14.56	32.72
12	1	14.52	33.32
15	1	14.18	33.03
18	1	14.36	32.74
21	1	14.37	32.93
24	1	14.28	32.93
27	1	14.24	32.75
30	1	14.28	32.64
33	1	14.03	32.78
36	1	14.24	32.99
39	1	14.07	32.80
42	1	14.09	32.95
45	1	13.97	33.00
48	1	13.91	33.11
51	1	13.94	33.27
54	1	14.67	32.88
57	1	13.94	32.93
60	1	13.93	33.00

Table S2. Recorded normal forces (in mN) for microgel packings of varying building block stiffnesses (E = 120 and 20 kPa, Ø = 55 µm) on the oscillatory rheometer throughout a time-sweep test with set measuring gap.

Microgel stiffness (kPa)	Normal force (mN)
2.5	11±6
20	46±11
65	41±15
120	23±10
165	30±11

Table S3. Recorded normal forces (in mN) for microgel packings of varying building block stiffnesses (Ø = 55 μm) on the oscillatory rheometer. Values are represented as mean ± s.d. (n=3).

	Microgel stiffness (kPa)	
Microgel size (μm)	20	120
25	37±13	23±11
55	46±11	23±10
75	46±12	12±2
100	27±7	17±8

Table S4. Recorded normal forces (in mN) for microgel packings of varying sizes on the oscillatory rheometer. Values are represented as mean ± s.d. (n=3).

Real diameter	Simulation Diameter	Spatial Coordinates						Simple Cubic			Random close packing		
$2R_0$	d	x	y	z	n_{sc}	n_{rcp}	$V_{particle}$	Total $V_{particle}$	Particle fraction	Porosity	Total $V_{particle}$	Particle fraction	Porosity
100	1	80.0	80.0	10.0	64000	78720	0.524	33510	0.524	0.476	41218	0.644	0.356
75	1	106.7	106.7	13.3	151419	186245	0.524	79283	0.524	0.476	97518	0.644	0.356
55	1	145.5	145.5	18.2	385299	473917	0.524	201742	0.524	0.476	248142	0.644	0.356
25	1	320.0	320.0	40.0	4096000	5038080	0.524	2144661	0.524	0.476	2637933	0.644	0.356

Table S5. Simulation parameters estimated for the generation of random close packings according to LS algorithm.

REFERENCES AND NOTES

1. L. Riley, L. Schirmer, T. Segura, Granular hydrogels: Emergent properties of jammed hydrogel microparticles and their applications in tissue repair and regeneration. *Curr. Opin. Biotechnol.* **60**, 1–8 (2019).

2. N. Kumar, S. Luding, Memory of jamming–multiscale models for soft and granular matter. *Granul. Matter* **18**, 58 (2016).

3. A. C. Daly, L. Riley, T. Segura, J. A. Burdick, Hydrogel microparticles for biomedical applications. *Nat. Rev. Mater.* **5**, 20–43 (2020).

4. N. F. Truong, E. Kurt, N. Tahmizyan, S. C. Lesher-Pérez, M. Chen, N. J. Darling, W. Xi, T. Segura, Microporous annealed particle hydrogel stiffness, void space size, and adhesion properties impact cell proliferation, cell spreading, and gene transfer. *Acta Biomater.* **94**, 160–172 (2019).

5. T. J. Hinton, Q. Jallerat, R. N. Palchesko, J. H. Park, M. S. Grodzicki, H.-J. Shue, M. H. Ramadan, A. R. Hudson, A. W. Feinberg, Three-dimensional printing of complex biological structures by freeform reversible embedding of suspended hydrogels. *Sci. Adv.* **1**, e1500758 (2015).

6. J. E. Mealy, J. J. Chung, H.-H. Jeong, D. Issadore, D. Lee, P. Atluri, J. A. Burdick, Injectable granular hydrogels with multifunctional properties for biomedical applications. *Adv. Mater.* **30**, 1705912 (2018).

7. T. Bhattacharjee, S. M. Zehnder, K. G. Rowe, S. Jain, R. M. Nixon, W. G. Sawyer, T. E. Angelini, Writing in the granular gel medium. *Sci. Adv.* **1**, e1500655 (2015).

8. D. R. Griffin, W. M. Weaver, P. O. Scumpia, D. Di Carlo, T. Segura, Accelerated wound healing by injectable microporous gel scaffolds assembled from annealed building blocks. *Nat. Mater.* **14**, 737–744 (2015).

9. F. Li, V. X. Truong, P. Fisch, C. Levinson, V. Glattauer, M. Zenobi-Wong, H. Thissen, J. S.

Forsythe, J. E. Frith, Cartilage tissue formation through assembly of microgels containing mesenchymal stem cells. *Acta Biomater.* **77**, 48–62 (2018).

10. J. Koh, D. R. Griffin, M. M. Archang, A. Feng, T. Horn, M. Margolis, D. Zalazar, T. Segura, P. O. Scumpia, D. Carlo, Enhanced in vivo delivery of stem cells using microporous annealed particle scaffolds. *Small* **15**, 1903147 (2019).

11. J. Fang, J. Koh, Q. Fang, H. Qiu, M. M. Archang, M. M. Hasani-Sadrabadi, H. Miwa, X. Zhong, R. Sievers, D. Gao, R. Lee, D. Di Carlo, S. Li, Injectable drug-releasing microporous annealed particle scaffolds for treating myocardial infarction. *Adv. Funct. Mater.* **30**, 2004307 (2020).

12. A. S. Caldwell, V. V. Rao, A. C. Golden, K. S. Anseth, Porous bio-click microgel scaffolds control hMSC interactions and promote their secretory properties. *Biomaterials* **232**, 119725 (2020).

13. L. R. Nih, E. Sideris, S. T. Carmichael, T. Segura, Injection of microporous annealing particle (MAP) hydrogels in the stroke cavity reduces gliosis and inflammation and promotes NPC migration to the lesion. *Adv. Mater.* **29**, 1606471 (2017).

14. S. Xin, O. M. Wyman, D. L. Alge, Assembly of PEG microgels into porous cell-instructive 3D scaffolds via thiol-ene click chemistry. *Adv. Healthc. Mater.* **7**, e1800160 (2018).

15. J. M. de Rutte, J. Koh, D. Di Carlo, Scalable high-throughput production of modular microgels for in situ assembly of microporous tissue scaffolds. *Adv. Funct. Mater.* **29**, 1900071 (2019).

16. A. S. Caldwell, G. T. Campbell, K. M. T. Shekiro, K. S. Anseth, Clickable microgel scaffolds as platforms for 3D cell encapsulation. *Adv. Healthc. Mater.* **6**, 1700254 (2017).

17. E. Sideris, D. R. Griffin, Y. Ding, S. Li, W. M. Weaver, D. Di Carlo, T. Hsiai, T. Segura, Particle hydrogels based on hyaluronic acid building blocks. *ACS Biomater Sci. Eng.* **2**, 2034–2041 (2016).

18. B. N. Pfaff, L. J. Pruett, N. J. Cornell, J. De Rutte, D. Di Carlo, C. B. Highley, D. R. Griffin,

Selective and improved photoannealing of microporous annealed particle (MAP) scaffolds. *ACS Biomater Sci. Eng.* **7**, 422–427 (2021).

19. K. L. Wilson, S. Cai, L. Pérez, M. M. Naffaa, S. H. Kelly, T. Segura, Stoichiometric post-modification of hydrogel microparticles dictates neural stem cell fate in microporous annealed particle scaffolds. *Adv. Mater.* **34**, e2201921 (2022).

20. S. R. Van Tomme, C. F. van Nostrum, M. Dijkstra, S. C. De Smedt, W. E. Hennink, Effect of particle size and charge on the network properties of microsphere-based hydrogels. *Eur. J. Pharm. Biopharm.* **70**, 522–530 (2008).

21. V. G. Muir, T. H. Qazi, J. Shan, J. Groll, J. A. Burdick, Influence of microgel fabrication technique on granular hydrogel properties. *ACS Biomater Sci. Eng.* **7**, 4269–4281 (2021).

22. M. Van Hecke, Jamming of soft particles: Geometry, mechanics, scaling and isostaticity. *J. Phys. Condens. Matter* **22**, 033101 (2010).

23. H. M. Jaeger, S. R. Nagel, R. P. Behringer, Granular solids, liquids, and gases. *Rev. Mod. Phys.* **68**, 1259–1273 (1996).

24. F. Radjai, J.-N. Roux, A. Daouadji, Modeling granular materials: Century-long research across scales. *J. Eng. Mech.* **143**, 04017002 (2017).

25. H. M. Shewan, G. E. Yakubov, M. R. Bonilla, J. R. Stokes, Viscoelasticity of non-colloidal hydrogel particle suspensions at the liquid–solid transition. *Soft Matter* **17**, 5073–5083 (2021).

26. J. Mattsson, H. M. Wyss, A. Fernandez-Nieves, K. Miyazaki, Z. Hu, D. R. Reichman, D. A. Weitz, Soft colloids make strong glasses. *Nature* **462**, 83–86 (2009).

27. K. van der Vaart, Y. Rahmani, R. Zargar, Z. Hu, D. Bonn, P. Schall, Rheology of concentrated soft and hard-sphere suspensions. *J. Rheol.* **57**, 1195–1209 (2013).

28. J. R. Seth, M. Cloitre, R. T. Bonnecaze, Elastic properties of soft particle pastes. *J. Rheol.* **50**, 353–376 (2006).

29. J. R. Seth, L. Mohan, C. Locatelli-Champagne, M. Cloitre, R. T. Bonnecaze, A micromechanical model to predict the flow of soft particle glasses. *Nat. Mater.* **10**, 838–843 (2011).

30. H. M. Jaeger, S. R. Nagel, R. P. Behringer, The physics of granular materials. *Phys. Today.* **49**, 32–38 (1996).

31. T. S. Majmudar, R. P. Behringer, Contact force measurements and stress-induced anisotropy in granular materials. *Nature* **435**, 1079–1082 (2005).

32. N. Brodu, J. A. Dijksman, R. P. Behringer, Spanning the scales of granular materials through microscopic force imaging. *Nat. Commun.* **6**, 6361 (2015).

33. C. Martino, D. Vigolo, X. Casadevall i Solvas, S. Stavrakis, A. J. DeMello, Real-time PEGDA-based microgel generation and encapsulation in microdroplets. *Adv. Mater. Technol.* **1**, 1600028 (2016).

34. S. Seiffert, D. A. Weitz, Microfluidic fabrication of smart microgels from macromolecular precursors. *Polymer* **51**, 5883–5889 (2010).

35. Z. Jiang, B. Xia, R. McBride, J. Oakey, A microfluidic-based cell encapsulation platform to achieve high long-term cell viability in photopolymerized PEGNB hydrogel microspheres. *J. Mater. Chem. B* **5**, 173–180 (2017).

36. A. Meister, M. Gabi, P. Behr, P. Studer, J. Vörös, P. Niedermann, J. Bitterli, J. Polesel-Maris, M. Liley, H. Heinzelmann, T. Zambelli, FluidFM: Combining atomic force microscopy and nanofluidics in a universal liquid delivery system for single cell applications and beyond. *Nano Lett.* **9**, 2501–2507 (2009).

37. P. Dörig, D. Ossola, A. M. Truong, M. Graf, F. Stauffer, J. Vörös, T. Zambelli, Exchangeable colloidal AFM probes for the quantification of irreversible and long-term interactions. *Biophys. J.* **105**, 463–472 (2013).

38. C. B. Highley, K. H. Song, A. C. Daly, J. A. Burdick, Jammed microgel inks for 3D printing

applications. *Adv. Sci.* **6**, 1801076 (2019).

39. T. Bhattacharjee, C. P. Kabb, C. S. O'Bryan, J. M. Urueña, B. S. Sumerlin, W. G. Sawyer, T. E. Angelini, Polyelectrolyte scaling laws for microgel yielding near jamming. *Soft Matter* **14**, 1559–1570 (2018).

40. S. Adams, W. J. Frith, J. R. Stokes, Influence of particle modulus on the rheological properties of agar microgel suspensions. *J. Rheol.* **48**, 1195–1213 (2004).

41. P. Menut, S. Seiffert, J. Sprakel, D. A. Weitz, Does size matter? Elasticity of compressed suspensions of colloidal- and granular-scale microgels. *Soft Matter* **8**, 156–164 (2012).

42. J. Gaume, H. Löwe, S. Tan, L. Tsang, Scaling laws for the mechanics of loose and cohesive granular materials based on Baxter's sticky hard spheres. *Phys. Rev. E.* **96**, 032914 (2017).

43. A. J. Liu, S. Ramaswamy, T. G. Mason, H. Gang, D. A. Weitz, Anomalous viscous loss in emulsions. *Phys. Rev. Lett.* **76**, 3017–3020 (1996).

44. S. Xin, D. Chimene, J. E. Garza, A. K. Gaharwar, D. L. Alge, Clickable PEG hydrogel microspheres as building blocks for 3D bioprinting. *Biomater. Sci.* **7**, 1179–1187 (2019).

45. M. Shin, K. H. Song, J. C. Burrell, D. K. Cullen, J. A. Burdick, Injectable and conductive granular hydrogels for 3D printing and electroactive tissue support. *Adv. Sci.* **6**, 1901229 (2019).

46. A. R. Payne, The dynamic properties of carbon black-loaded natural rubber vulcanizates. Part I. *J. Appl. Polym. Sci.* **6**, 57–63 (1962).

47. X. Fan, H. Xu, Q. Zhang, D. Xiao, Y. Song, Q. Zheng, Insight into the weak strain overshoot of carbon black filled natural rubber. *Polymer* **167**, 109–117 (2019).

48. A. Agrawal, H.-Y. Yu, S. Srivastava, S. Choudhury, S. Narayanan, L. A. Archer, Dynamics and yielding of binary self-suspended nanoparticle fluids. *Soft Matter* **11**, 5224–5234 (2015).

49. A. C. Yu, A. A. A. Smith, E. A. Appel, Structural considerations for physical hydrogels based on polymer–nanoparticle interactions. *Mol. Syst. Des. Eng.* **5**, 401–407 (2020).

50. G. J. Donley, P. K. Singh, A. Shetty, S. A. Rogers, Elucidating the G″ overshoot in soft materials with a yield transition via a time-resolved experimental strain decomposition. *Proc. Natl. Acad. Sci.* **117**, 21945–21952 (2020).

51. G. J. Donley, J. R. de Bruyn, G. H. McKinley, S. A. Rogers, Time-resolved dynamics of the yielding transition in soft materials. *J. Nonnewton. Fluid Mech.* **264**, 117–134 (2019).

52. Q. Sun, G. Wang, K. Hu, Some open problems in granular matter mechanics. *Prog. Nat. Sci.* **19**, 523–529 (2009).

53. K. Walton, The effective elastic moduli of a random packing of spheres. *J. Mech. Phys. Solids* **35**, 213–226 (1987).

54. H. Hertz, On the contact of elastic solids. *J. Reine Angew. Math.* **92**, 156–171 (1881).

55. L. Rovigatti, N. Gnan, A. Ninarello, E. Zaccarelli, Connecting elasticity and effective interactions of neutral microgels: The validity of the Hertzian model. *Macromolecules* **52**, 4895–4906 (2019).

56. F. Radjai, S. Roux, J. J. Moreau, Contact forces in a granular packing. *Chaos* **9**, 544–550 (1999).

57. N. P. Kruyt, On weak and strong contact force networks in granular materials. *Int. J. Solids Struct.* **92–93**, 135–140 (2016).

58. F. Radjai, D. E. Wolf, M. Jean, J.-J. Moreau, Bimodal character of stress transmission in granular packings. *Phys. Rev. Lett.* **80**, 61 (1998).

59. K. L. Johnson, *Contact Mechanics* (Cambridge University Press, 1985).

60. C. S. O'Hern, L. E. Silbert, A. J. Liu, S. R. Nagel, Jamming at zero temperature and zero applied stress: The epitome of disorder. *Phys. Rev. E.* **68**, 011306 (2003).

61. J. G. Berryman, Random close packing of hard spheres and disks. *Phys. Rev. A* **27**, 1053–1061 (1983).

62. H. A. Makse, D. L. Johnson, L. M. Schwartz, Packing of compressible granular materials. *Phys. Rev. Lett.* **84**, 4160–4163 (2000).

63. V. Baranau, U. Tallarek, Random-close packing limits for monodisperse and polydisperse hard spheres. *Soft Matter* **10**, 3826–3841 (2014).

64. L. Mohan, R. T. Bonnecaze, Short-ranged pair distribution function for concentrated suspensions of soft particles. *Soft Matter* **8**, 4216 (2012).

65. R. Zwanzig, R. D. Mountain, High-frequency elastic moduli of simple fluids. *J. Chem. Phys.* **43**, 4464–4471 (1965).

66. I. D. Evans, A. Lips, Concentration dependence of the linear elastic behaviour of model microgel dispersions. *J. Chem. Soc. Faraday Trans.* **86**, 3413 (1990).

67. J. Buitenhuis, S. Förster, Block copolymer micelles: Viscoelasticity and interaction potential of soft spheres. *J. Chem. Phys.* **107**, 262–272 (1997).

68. S. Xin, K. A. Deo, J. Dai, N. K. R. Pandian, D. Chimene, R. M. Moebius, A. Jain, A. Han, A. K. Gaharwar, D. L. Alge, Generalizing hydrogel microparticles into a new class of bioinks for extrusion bioprinting. *Sci. Adv.* **7**, 3087–3102 (2021).

69. R. Buscall, Effect of long-range repulsive forces on the viscosity of concentrated latices: Comparison of experimental data with an effective hard-sphere model. *J. Chem. Soc. Faraday Trans.* **87**, 1365–1370 (1991).

70. N. Paxton, W. Smolan, T. Böck, F. Melchels, J. Groll, T. Jungst, Proposal to assess printability of bioinks for extrusion-based bioprinting and evaluation of rheological properties governing bioprintability. *Biofabrication* **9**, 044107 (2017).

71. C. W. Macminn, E. R. Dufresne, J. S. Wettlaufer, Large deformations of a soft porous material. *Phys. Rev. Appl.* **5**, 044020 (2016).

72. Y. Hu, X. Zhao, J. J. Vlassak, Z. Suo, Using indentation to characterize the poroelasticity of

gels. *Appl. Phys. Lett.* **96**, 121904 (2010).

73. S. C. Tsai, D. Botts, J. Plouff, Effects of particle properties on the rheology of concentrated noncolloidal suspensions. *J. Rheol.* **36**, 1291–1305 (1992).

74. M. Glaubitz, N. Medvedev, D. Pussak, L. Hartmann, S. Schmidt, C. A. Helm, M. Delcea, A novel contact model for AFM indentation experiments on soft spherical cell-like particles. *Soft Matter* **10**, 6732–6741 (2014).

75. P. Rosendahl, K. Plak, A. Jacobi, M. Kraeter, N. Toepfner, O. Otto, C. Herold, M. Winzi, M. Herbig, Y. Ge, S. Girardo, K. Wagner, B. Baum, J. Guck, Real-time fluorescence and deformability cytometry. *Nat. Methods* **15**, 355–358 (2018).

76. J. A. Dijksman, N. Brodu, R. P. Behringer, Refractive index matched scanning and detection of soft particles. *Rev. Sci. Instrum.* **88**, 051807 (2017).

77. O. Y. Dudaryeva, A. Bucciarelli, G. Bovone, F. Huwyler, S. Jaydev, N. Broguiere, M. Al-Bayati, M. Lütolf, M. W. Tibbitt, O. Y. Dudaryeva, A. Bucciarelli, G. Bovone, F. Huwyler, S. Jaydev, N. Broguiere, M. Al-Bayati, M. Lütolf, M. W. Tibbitt, 3D confinement regulates cell life and death. *Adv. Funct. Mater.* **31**, 2104098 (2021).

78. S. Cárdenas-Pérez, J. J. Chanona-Pérez, J. V. Méndez-Méndez, I. Arzate-Vázquez, J. D. Hernández-Varela, N. G. Vera, Recent advances in atomic force microscopy for assessing the nanomechanical properties of food materials. *Trends Food Sci. Technol.* **87**, 59–72 (2019).

79. N. Koumakis, G. Petekidis, Two step yielding in attractive colloids: Transition from gels to attractive glasses. *Soft Matter* **7**, 2456–2470 (2011).

80. R. H. Ewoldt, P. Winter, J. Maxey, G. H. McKinley, Large amplitude oscillatory shear of pseudoplastic and elastoviscoplastic materials. *Rheol. Acta.* **49**, 191–212 (2010).

81. M. Rubinstein, R. H. Colby, *Polymers Physics* (Oxford Univ. Press, 2003).

82. Y. Akagi, T. Matsunaga, M. Shibayama, U. Chung, T. Sakai, Evaluation of topological defects

in tetra-PEG gels. *Macromolecules* **43**, 488–493 (2010).

83. I. Bouhid de Aguiar, K. Schroën, M. Meireles, A. Bouchoux, Compressive resistance of granular-scale microgels: From loose to dense packing. *Colloids Surf. A Physicochem. Eng. Asp.* **553**, 406–416 (2018).

84. L. E. Silbert, Jamming of frictional spheres and random loose packing. *Soft Matter* **6**, 2918–2924 (2010).

85. J. D. Bernal, J. Mason, Packing of spheres: Co-ordination of randomly packed spheres. *Nature* **188**, 910–911 (1960).

86. G. M. Conley, C. Zhang, P. Aebischer, J. L. Harden, F. Scheffold, Relationship between rheology and structure of interpenetrating, deforming and compressing microgels. *Nat. Commun.* **10**, 2436 (2019).

87. V. Baranau, U. Tallarek, On the jamming phase diagram for frictionless hard-sphere packings. *Soft Matter* **10**, 7838–7848 (2014).

88. S. L. Elliott, W. B. Russel, High frequency shear modulus of polymerically stabilized colloids. *J. Rheol.* **42**, 361 (1998).